University of Alberta

Skin Dose in Longitudinal and Transverse Linac-MRIs using Monte-Carlo
and realistic 3D MRI field models

by

Amirmohamad Keyvanloo Shahrestanaky

A thesis submitted to the Faculty of Graduate Studies and Research
in partial fulfillment of the requirements for the degree of

Master of Science

in

Medical Physics

Department of Oncology

©Amirmohamad Keyvanloo Shahrestanaky

Spring 2013
Edmonton, Alberta

ABSTRACT

The integration of a clinical linear accelerator (linac) with a magnetic resonance imaging (MRI) system would provide real-time tumor tracking. The magnetic fields of linac-MR systems modify the path of contaminant electrons in photon beams, which alters patient skin dose. In this work, we used Monte Carlo calculations that incorporate realistic 3D magnetic field models of longitudinal and transverse linac-MR systems to accurately quantify the changes in skin dose. The results show that fringe fields of realistic 3D B-fields decay rapidly and have a very small magnitude at the linac's head. As a result, for longitudinal linac-MR systems only a small increase in the entrance skin dose is predicted. For transverse linac-MR systems, changes to the entrance skin dose are small for most scenarios. On the exit side, however, a fairly large increase is observed for perpendicular beams due to the electron return effect, but significantly drops for large oblique angles of incidence.

TABLE OF CONTENTS

List of Figures

CHAPTER 1 : INTRODUCTION

1.1 ADVANCES IN RADIOTHERAPY

Radiation treatment of cancer started shortly after the discovery of the X-ray by W. C. Röntgen in 1895.[1,2] A few months later, in 1896, the French physicist Henry Becquerel discovered natural radioactivity,[3] and two years later in 1898 radium was discovered by the Curies.[4] With these three major discoveries a new era in science and medicine emerged with much focus on the treatment of cancer by means of ionizing radiation. Emil Grubbe was the first person who used X-rays to treat cancer in January 1896 in Chicago,[3] and in 1899 the first cancer patient cured by radiotherapy was reported.[4] First X-rays were produced by the Crookes tube,[1] a vacuum glass tube containing a cold cathode and an anode. Electrons were liberated from the cathode and were accelerated towards the anode through a potential difference. The electron beam, called cathode rays, impinged onto the anode to produce X-rays primarily through Bremsstrahlung interactions.[5] The X-rays used in early radiotherapy treatments, however, had low peak energies of < 100 kVp with limited therapeutic effect. Because the dose deposited declined rapidly with increasing depth in the patient for these low energy beams, mainly superficial lesions could be treated[6]. Furthermore, most treatments suffered from inaccuracies in the delivery of radiation[6] and from long exposure times.[2,6] As a result, severe skin reactions and damage to surrounding soft tissues

were limiting the treatment of deep-seated tumors. Multiple radiation field techniques introduced by Dr. Béclère later in 1908 proved somewhat promising in the treatment of such tumors.[7]

Initial progress in the field of radiotherapy in the first few decades of the 20th century was largely driven by physicists trying to understand the interaction of radiation with body tissues and to produce X-rays more efficiently and with higher peak energy.[3] In 1913, William Coolidge developed the hot-cathode tube[3,6,8] which used stronger vacuum and thermionic electron emission. Coolidge tubes were capable of producing X-rays with a peak energy of 140 kVp,[6] which was sufficient for diagnostic purposes.[5,6] A few years later, peak X-ray energies were increased to 400 kVp and the so called ortho-voltage treatment of deep-seated tumors made possible. Thereafter, for more than twenty years, ortho-voltage X-rays and radium were the only sources of high energy photons for the treatment of cancer. Radium was used in different ways: by direct application, in brachytherapy (interstitial or body cavity insertion) units,[3] or in teleradium units.[9] Further technological advancements in radiation therapy led to treatment units with 1 megavolt (MV) beam energies, which were suitable for the treatment of tumors at greater depths. These units used a 30-foot evacuated X-ray tube and a Cockcrott-Walton high voltage direct-current generator maintaining a potential difference of 1 MV across the X-ray tube.[10] In 1937 the first megavolt treatment unit was used for patient treatment in the St. Bartholomew's Hospital , London.[11] By 1940, it was well established that treatment beams with megavoltage energies

offer great advantages for radiation treatment of deep-seated tumors.[11,12] In addition to their greater penetrating ability, these beams offered a skin-sparing benefit: in contrast to kilovoltage beams, the entrance dose of megavoltage beams was significantly reduced from the maximum dose, which occurred at a depth beyond the sensitive skin layers.

In addition to the progress in achieving higher quality (*i.e.* energy) X-rays, the beginning of the 1900's had already seen the first side effects of the exposure to radiation: radiation induced leukemia, lost fingers and skin ulcerations being reported.[3] Soon it was realized that normal tissues should be differentiated from the tumor tissues with respect to their response to radiation. The field of radiobiology was then born of a need to understand the effects of radiation at a cellular level.[3] During the 1940's radiation oncology emerged as a multidisciplinary field where physicists, biologists, chemists, and radiation oncologists[3] extensively worked together to better understand the effects of radiation on living tissue. This union of scientific disciplines introduced concepts such as depth-dose and isodose diagrams,[13] identified the benefits of fractionated radiotherapy, and discovered correlations between radio-sensitivity and oxygenation.[3]

In 1940 Donald W. Kerst developed the betatron at the University of Illinois, which enabled the step to the next level of treatment beam energies.[10,14] The betatron accelerated electrons cyclically via an increasing magnetic flux,

producing a nearly monoenergetic electron beam.[10,14] At first, a beam energy of 2.3 MeV was produced and later electrons were accelerated to energies of 300 MeV.[10,14] In 1948, the first patient was successfully treated with the betatron by mounting an X-ray target on the injector assembly.[10] In the same year the first medical linear accelerator was developed by D. W. Fry as an alternative means of generating MV X-ray beams for radiotherapy treatments. These early linear accelerators used megawatt microwave generators called magnetrons, which were originally developed in England for radar during World War II[10,15] Afterward, advances in klystron technology meant that these devices could also be used in megawatt microwave power generation. Both magnetrons and klystrons were key to the development of the next generation of medical linacs in the 1960's that featured X-ray beam energies of up to 25 MV.[6]

In the late 1940's, prior to the emergence of medical linacs, high energy teletherapy units using cobalt-60 (^{60}Co) radionuclide sources were developed as a means of producing megavoltage photon beams.[3,5,6] Cobalt-60 is a radionuclidethat is artificially created through the neutron irradiation of ^{59}Co. It emits gamma rays with a mean photon energy of 1.25 MeV,[6] a sufficiently high energy to have a skin sparing effect during treatment.[10] Harold Johns and his group developed the first therapy unit with cobalt-60 in Saskatoon and the first patient was treated with it in 1951 in London Ontario, Canada.[6] Although for decades cobalt-60 had been the gold standard teletherapy unit for its robustness,

ease of use and relatively low maintenance, it has been gradually superseded by the higher energy linear accelerators (linacs).

After the development of medical linacs and ^{60}Co units, complicated field shaping devices[16,17] were developed to make the treatment beam conform to the tumor shape. In the 1970's computed tomography (CT) was also introduced which allowed for three dimensional (3D) delineation of tumor and critical structure volumes. This motivated the creation of advanced 3D treatment planning systems that could utilize CT's ability to accurately determine the electron densities of different tissues for individualized radiation dose calculations. These advances in computer technologies made conformal treatments using multiple radiation beams possible,[3] leading to the development of 3D conformal radiotherapy (3D CRT) in the 1970s and dose escalation techniques, such as intensity-modulated radiotherapy (IMRT),[6,18] in the 1980s. The incorporation of computer-controlled multileaf collimation (MLC) into the linacs made implementation of CRT and IMRT techniques convenient. The accuracy provided by these conformal techniques offered greater sparing of normal tissues[3,6] and thus reductions in normal tissue complications probabilities (NTCP).[6] Exploiting this, dose escalation techniques could then potentially achieve higher tumor control probability (TCP) while maintaining acceptable NTCPs. In the last twenty years techniques to further optimize conformal dose distributions have included tomotherapy, treatment gating, and adaptive radiation treatment (ART).[6]

While advanced 3D treatment planning and accurate delivery techniques (3D CRT and IMRT) promised greater tumor control and eradication[6,19,20] with fewer complications, it had early been recognized that the full realization of this potential critically depended on the quality of the imaging used at different stages of the radiotherapy process. A first factor is the accuracy of the contouring differentiating between diseased tissue and the critical structures surrounding it on the 3D images used for treatment planning. While CT data is ideal for dose calculation purposes in the presence of tissue heterogeneities, it suffers from poor soft-tissue contrast. The introduction of magnetic resonance imaging (MRI) in radiation oncology offers significant improvement in tumor and normal tissue delineation.[3] The excellent soft-tissue contrast inherent in MRI images has allowed for the diagnosis and localization of malignancies to an unprecedented level.[6] A second critical component to advanced radiotherapy techniques is the accuracy and reproducibility of the patient setup with respect to the treatment beams during the course of fractionated radiation therapy. Reproducibility of patient setup is essential to reduce the treatment margins around the tumor that are used to account for patient setup uncertainty, and hence to spare normal tissues surrounding the tumor.[3,19,20] Thus, there has been significant effort to improve the image guidance techniques used for daily localization of tumor and critical structures.[3]

1.2   IMAGE-GUIDED RADIOTHERAPY (IGRT)

As discussed, a major goal in external beam radiotherapy (XBRT) is to deliver the highest possible dose to malignant tissues, while sparing surrounding critical structures. This will result in the greatest therapeutic gain, where high probability of tumor control and low likelihood of normal tissue complications are obtained. Achieving this goal, however, is limited by difficulties in exact delineation of diseased volume from the healthy tissues as well as uncertainties in the positioning of the target/tumor with respect to the treatment beams.   In fractionated XBRT, positioning uncertainties can occur both during a treatment session (intrafractional) and over the course of the treatment (interfractional). The uncertainties during treatment delivery typically arise from the anatomical changes due to respiration, cardiac motion, swallowing, and bowel movements. Interfractional uncertainties, on the other hand, arise from irreproducibility of daily patient setup (setup error) and physiological changes, such as tumor shrinkage, weight loss, and the filling status of internal organs.

International Commission of Radiation Units and Measurements (ICRU) reports ICRU 50[21,22] and ICRU 62[23] provide guidelines that define volumes and margins to account for these uncertainties (Fig. 1.1). The gross tumor volume (GTV) is contoured from the patient's planning images and is defined as the volume containing the palpable extent of the cancerous tissue detectable from the planning images.[21] The GTV is then expanded to a larger dose volume called the

7

clinical target volume (CTV) to encompass the GTV and any microscopic spread of the tumor cells that are not detectable in the planning images.[21] In order to account for intra- and interfractional positioning uncertainties the internal margin (IM) and setup margin (SM) are introduced, respectively, and the CTV is in turn expanded to a larger volume called the planning target volume (PTV).[21,23] The prescribed dose is then delivered to the PTV to hopefully guarantee the eradication of all tumor cells. Inevitably, any healthy tissue within the PTV is also unnecessarily irradiated, which can lead to an increases likelihood of normal tissue complications and secondary disease.
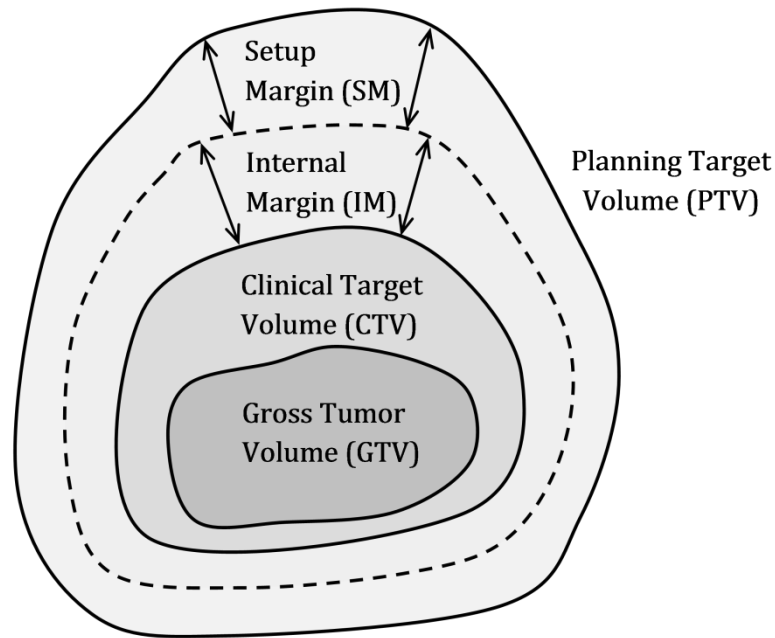
Figure 1.1: Schematic illustration of the patient dose margins defined during radiotherapy treatment planning. The internal margin (IM) and setup margin (SM) account for positioning uncertainties arising from intrafractional and interfractional variations in the patient anatomy, respectively.

Much effort has been made to reduce the CTV-to-PTV margin by reducing both the IM and SM, with the goal of reducing normal tissue complications. To reduce the IM, researchers have tried to quantify organ motion and incorporate it into the treatment planning process through various schemes such as respiratory gating and mathematical modeling of breathing and motion.[24-27] Furthermore, the advanced practice of image-guided radiotherapy (IGRT) has helped reduce the SM margin by frequently imaging the patient prior to, and possibly during and after the treatment. The images are compared with either the 3D planning CT data or 2D digitally reconstructed radiographs (DRRs) derived from this CT data set to account for daily setup variations or to calculate changes in the setup that occurred over the course of the treatment. Appropriate linear shifts can then be made to the position of the patient couch; more recently, specialized couches with multiple rotational degrees of freedom may be used to allow incorporation of rotations in the shift parameters.

There are several different imaging modalities that have been developed for IGRT to help reduce interfractional positioning uncertainties.[19,20] A common such modality is the electronic portal imaging device (EPID) that is integrated on-board with a linear accelerator. The EPID is a planar imaging device which is positioned opposite a linac so as to utilize the megavoltage (MV) treatment beam to obtain a two-dimensional (2D) projection image of the patient in the treatment position.[28] Some linacs also allow this assembly to be rotated around the patient to obtain a series of projections that can be reconstructed into a volumetric MV

cone-beam computed tomography (CT) data set.[29,30] The images obtained by an EPID (2D or 3D) are used for pre-treatment patient setup verification. EPIDs can also be used as a dosimeter, either for monitoring the dose received by the patient during treatments, or for measuring the fluence of IMRT fields prior to delivery of the first patient treatment. Hence the EPID provides a useful quality assurance and treatment verification tool for IMRT.[19,28,31,32]

Since the EPID uses MV X-rays, images obtained by this modality suffer from poor contrast and overlaying of 3D structures onto 2D planes. These issues have been circumvented by introducing an on-board kilovoltage (kV) X-ray tube and an amorphous silicon flat panel detector, which are mounted orthogonal to the treatment beam and rotate with the linac.[33,34] Prior to the treatment, the gantry is rotated around the patient acquiring many cone-beam computed tomography (CBCT) data projections in 2D; a volumetric image with superior spatial resolution and soft-tissue contrast is then reconstructed in 3D using cone-beam computed tomography (CBCT) reconstruction methods.

Another widely-used IGRT modality is helical TomoTherapy, which uses the concept of combining a 6 MV linac with a spiral megavoltage CT imager.[35] The assembly is mounted on a ring-based gantry and rotates (at speeds much faster than a conventional linac) around the patient as the patient couch is slowly translated through the bore of the machine. The kV X-ray tube in the CT scanner has been replaced with 3.5 MV photon beam to help reduce artifacts that are

caused by high atomic number materials such as metal prostheses.[30] The TomoTherapy system performs helical IMRT which enables highly conformal dose distributions to be delivered to the patient.[36] This modality allows for single-slice or volumetric MVCT imaging of the patient to be used for patient setup and treatment verification purposes.[37,38] The MVCT images obtained by the tomotherapy unit, though 3D, suffer from poor soft tissue contrast due to the use of MV photon beams.

In addition to the poor soft tissue contrast of many of the aforementioned IGRT imaging modalities, a major shortcoming with all of them is that acquiring three-dimensional (3D) images is restricted to immediately before or after the treatment session. Real-time imaging is thus not possible. There are fluoroscopy-based tracking systems, such as implemented on Cyberknife[39], that are capable of indirectly tracking tumor motion in real-time through radiographic tracking[40] of implanted fiducial markers. A drawback of such a technique is that 3D, tomographic, image sets are not utilized. Several other IGRT techniques exist that do not rely on radiographic imaging. The most common of these alternatives are electromagnetic field tracking[41] of radio-frequency transponders implanted into the tumor, optical tracking[42] of external surrogates (infrared reflectors), and ultrasonography (US). The US is a non-invasive technique which is suitable for effective visualization of soft-tissue anatomy that is unobstructed by gas or bone. It has mostly been used for target localization prior to treatment of prostate and other abdominal malignancies.[43] The major drawbacks of the first two techniques

involve the inability to visualize the target volume in real-time, as well as the difficulty of calibrating the detection systems for accurate target positioning. The US modality suffers from poor image quality, although 3D robotic US is being explored for real-time imaging of the prostate motion.

1.3 MAGNETIC RESONANCE IMAGING AND REAL-TIME IGRT

Most current IGRT techniques rely on daily images of the patient obtained before or after the treatment to help minimize setup errors. These techniques, however, are not capable of real-time tumor tracking and hence do not deal with intrafractional positioning uncertainties such as tumor/organ motion. Consequently a fairly large CTV-to-PTV margin is still needed to cover the full extent of the tumor motion and to ensure that all the tumor cells are adequately irradiated. In order to address the shortcomings of current IGRT techniques a few groups around the world are pursuing the integration of a magnetic resonance imaging (MRI) scanner with an external beam treatment unit such as a linac or ^{60}Co unit.[44-50] MRI offers exceptional advantages over X-ray based IGRT techniques: 1) it provides exquisite soft-tissue contrast suitable for the visualization and delineation of tumors and organs at risk (OAR) in cancer patients; 2) it is capable of rapidly acquiring volumetric images without the need of rotation, allowing for near real-time monitoring of target motion in 3D without

interrupting radiation delivery; and 3) there is no ionizing radiation associated with MRI imaging and is thus considered safe to the patient. Guidance of an MLC by 3D MRI images obtained in real-time enables shaping of the treatment beam to closely conform to and follow the tumor during a treatment. This will result in a reduction of treatment errors and the margins associated with interfractional positioning and intrafractional target motion. Hence, improved treatment outcomes may be achieved.

1.4 LINAC-MR AT THE CROSS CANCER INSTITUTE

Currently there are two working prototype linac-MR systems that would allow for patient imaging in real-time, providing soft-tissue contrast suitable for real-time tumor tracking.[46,48,49] The linac-MR prototype described in Ref. [49] employs a split-solenoid cylindrical MRI system that generates a main magnetic (B) field along the superior-inferior patient axis and transverse (i.e. perpendicular) to the linac's X-ray beam. Our research group at the Cross Cancer Institute (CCI) in Edmonton, AB, Canada, proposed a Linac-MR design [Ref. 46, 48] where a bi-planar low field magnet MRI is coupled with a 6 MV linac. The entire integrated assembly is able to rotate around the patient. The rotating bi-planar (RBP) system produces a main MRI magnetic field perpendicular to the head-foot patient axis with two possible orientations of the linac's X-ray beam direction relative to the B-field: perpendicular for the transverse configuration,[51] and parallel in the longitudinal configuration[52].

In the transverse RBP configuration, Fig. 1.2, the linac is mounted on the open end of the biplanar magnet such that the treatment beam is oriented perpendicular to the main B-field, and the radiation beam can reach the patient unobstructed at any gantry angle.[51]
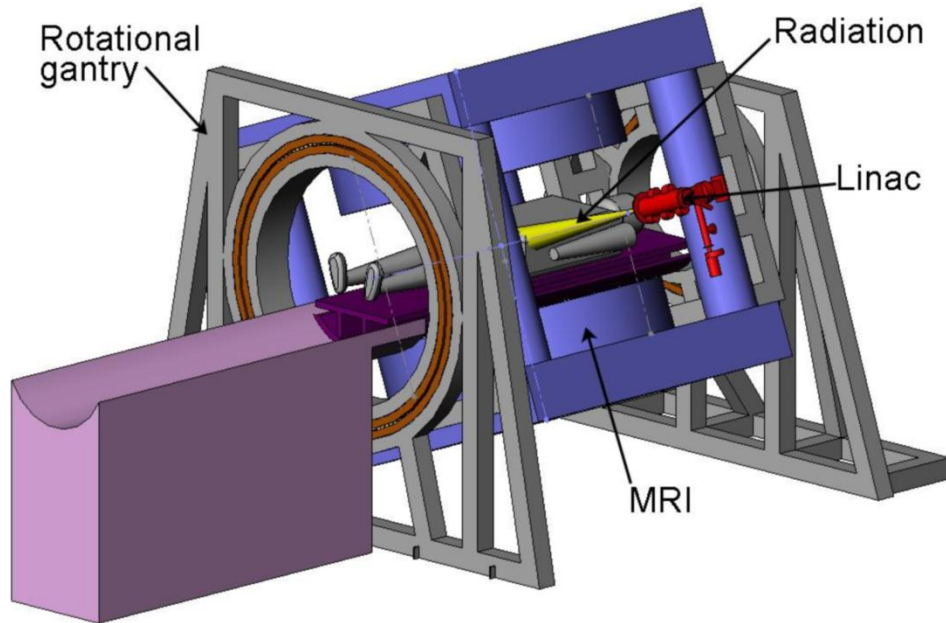
Figure 1.2: Transverse configuration of the CCI Linac-MR system.

Our research group has constructed a small-scale prototype transverse linac-MR system, where a 27.5 cm gap, 0.2 T biplanar permanent magnet MRI scanner is integrated to a refurbished 6 MV linac and mounted on a stationary gantry. The first ever MR images during megavoltage photon irradiation was obtained at the Cross Cancer Institute using this prototype.[51] In the alternative longitudinal RBP configuration, Fig. 1.3, the linac is mounted exterior to the MRI magnet with the

treatment beam irradiating the patient through a hole (referred to as "air column")
in one of the magnet poles along the magnet's axis of symmetry (i.e. parallel to
the B-field). Similar to the transverse configuration, the magnet and linac rotate
together on the same gantry.
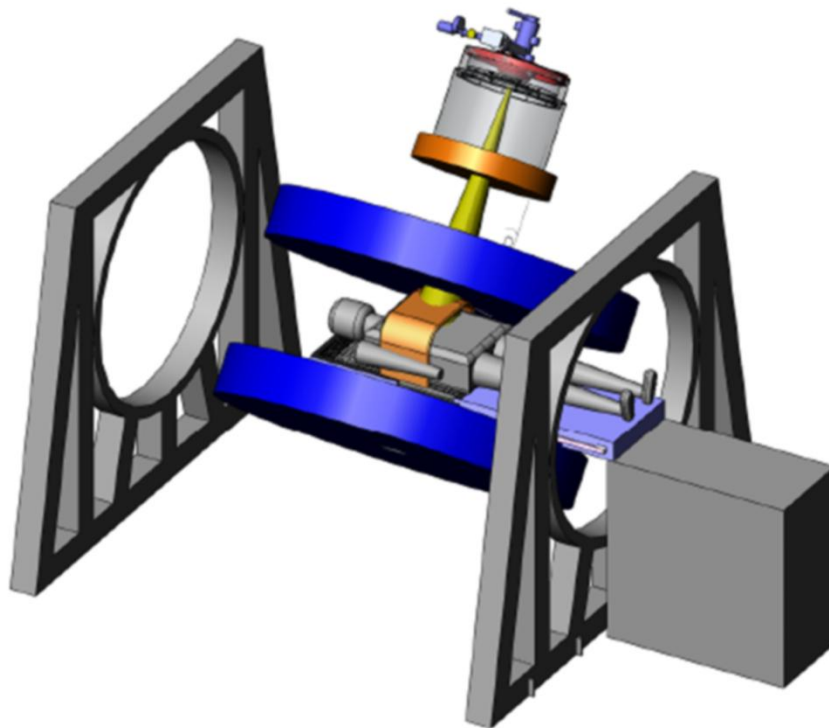
Figure 1.3: Longitudinal configuration of the CCI Linac-MR system.

The coupling of the magnetic field of an MRI scanner with a linac results in many
design challenges. Dosimetric issues are introduced since the magnetic field will
alter the path of contaminant electrons, as well as the secondary electrons in the
patient. Furthermore, the B-field can interfere with the linac waveguide and

compromise its functionality and efficiency. Our group has been investigating these issues and has identified solutions for many of them. The work presented in this thesis deals with quantifying the changes in the skin dose caused by the B-field of both linac-MR configurations.

1.5 RESEARCH MOTIVATION

It has been established that Linac-MRI systems with transverse geometry may suffer from significant dose perturbations within the patient, particularly when higher magnetic field strengths are used. These perturbations are caused by several effects related to the direction of the Lorentz force acting on high energy electrons. These effects include changes to percentage depth-dose, lateral shifts in dose distributions, and electron return effects (ERE) that increase exit dose and cause cold and hot spots at lung/tissue interfaces.[51,53-55] With a longitudinal geometry many of these dosimetric issues within the patient are eliminated, since the Lorentz force instead restricts the radial spread of secondary electrons in the patient when the B-field is parallel to the photon beam axis.[56,57] Use of a parallel magnetic field also reduces the penumbral width.[56,58] Further, in a recent study Kirkby *et al.*[52] showed that the longitudinal rotating bi-planar system exhibits an increase in the dose to the planning target volume (PTV), potentially offering reduced normal tissue dose for the same PTV dose. This effect is more pronounced for higher magnetic field strengths and in low density tissue such as lung.

16

Another potentially important aspect of linac-MR dosimetry is the impact on patient skin dose. The main contribution to skin dose at the beam entrance comes from the contaminant electrons present in megavoltage photon beams. The magnetic field of the MRI unit perturbs the fluence of contaminant electrons and hence alters the skin dose in both linac-MR configurations. In a transverse system the Lorentz force sweeps the contaminants away from the incident path of the X-ray beam and a reduction in the skin dose would be expected. Changes in the entrance and exit doses from a transverse magnetic field in a fixed cylindrical MRI geometry have been studied extensively.[59-61] On the entry side, the central axis (CAX) skin dose is less than that for the zero magnetic field case for negative surface orientations (see Fig. 1 in Ref. [61] for the sense of orientation), but increases strongly for large positive angles. The Lorentz force on secondary electrons in the phantom causes a lateral ERE to occur on the entry side, which provides a possible explanation for this increase in skin dose. For magnetic fields less than 0.6 T, the ERE increases exit surface dose irrespective of exit surface orientation. However, at higher magnetic field strengths and for large surface angles, the exit skin dose tends to be lower than the zero field case. The entrance and exit dose have not yet been investigated for the transverse RBP configuration. While in the fixed cylindrical system the Lorentz force acts perpendicular to the head-foot axis of the patient, in the rotating bi-planar system it acts parallel to the patient axis. Thus, differences in the effects of the transverse magnetic field on the entrance and exit doses are expected.

17

The exit dose does not increase in the longitudinal linac-MR configuration since the exiting electrons are merely confined within the exiting beam and do not return back to the surface. However, increase in the entry skin dose, within the area of the beam, is potentially of particular concern for this geometry, since the Lorentz force will act to confine the contaminant electrons and direct them to the patient surface with reduced lateral spread. Oborn *et al.*[62] quantified changes in entry skin dose for various hypothetical 1-D uniform and fringe magnetic fields that were incorporated into Monte Carlo dose calculations. Their results showed that the skin dose in a parallel linac-MR configuration strongly depends on the spatial characteristics of the fringe field extending into the linac's beam collimation system. For a 1.0 T MRI with a main field that extends up to the linac head, their simulations predicted a wide range of skin doses for various fringe-field scenarios: ~80% of D_{max} when the fringe field is zero ; nearly equal to the D_{max} dose for a uniform fringe field of 0.06 T extending to the source; and a drastic increase up to 400-500% of D_{max} when the fringe field was modeled exterior to the magnet as decreasing from 1.0 T according to a $1/r^2$ relationship. The extreme range of skin doses reported by Oborn *et al.*[62] means that the significance of skin dose increases in a longitudinal linac-MR can only be determined with further comprehensive investigation based on a more definite determination of the fringe fields. The magnetic fields modeled in their work were generally unrealistic for three reasons: 1) the large extension of the uniform MRI field to the linac head is unnecessary and impractical from a design perspective;

18

2) the fringe fields are much too large as a result of the effects of the yoke and magnetic shields not being incorporated in their models; and 3) no transverse (x and y) components of the B-fields were considered.

In this work, we report on the entry and exit skin dose for linac-MRI system based on RBP geometry. Firstly, we calculate realistic model magnetic fields of several magnet designs, using Finite Element Method (FEM), to determine the characteristics of realistic fringe fields. Secondly, by using the realistic 3D magnetic fields, we accurately predict the increase in skin dose in a longitudinal RBP linac-MR system and the changes in entrance and exit skin doses in a transverse RBP linac-MR system. These changes are quantified for various field sizes, for various air gaps between the phantom and the magnet pole (longitudinal case), and for various angles of obliquity of the incident beam relative to the patient surface (transverse case). All dosimetric simulations were performed using EGSnrc Monte Carlo codes that were modified to include vector magnetic fields.

1.6 REFERENCES

1. W. C. Roentgen. "On a New Kind of Rays", Nature, **53**, 274–276, (1896).

2. O. Glasser. *Wilhelm Conrad Rontgen and the Early History of the Roentgen Rays* (C. C. Thomas, Illinois, 1934).

3. J. Bernier, E.J. Hall, and A. Giaccia, *Radiation oncology: a century of achievements*, Nature Reviews Cancer **4**, 737–747, 2004.

4. C.A. Perez, L.W. Brady, J.L. Roti "Overview" *Principles and Practice of Radiation Oncology 3rd Edition*, Editors: C.A. Perez and L.W. Brady, Philadelphia, PA: Lippincott-Raven, pp.1–78, 1998.

5. H. E. Johns and J. R. Cunningham. *The Physics of Radiology* (C. C. Thomas, Illinois, 1983).

6. J. V. Dyk. *The Modern Technology of Radiation Oncology* (Medical Physics Publishing, Wisconsin, 1999 & 2005).

7. A. B. Wayte. "Treatment of Some Disorders of the Pituitary by Radiotherapy", Proc R Soc Med, **44**, 450–452, (1951).

8. W. D. Coolidge. United States Patent Office. (1934) *X-ray Tube,* US Patent 1946312.

9. E. Lysholm, *Apparatus for the production of a narrow beam of rays in treatment by radium at a distance*, Acta Radiologica, 2, 516–519, 1923.

10. J. S. Laughlin. "Development of the technology of radiation therapy". Radiographics, **9**, 1245–1266, (1989).

11. G. S. Innes. "The one million volt X-ray therapy equipment at St. Bartholomew's Hospital", Br. J. Radiol., **22** (suppl), 11–16, (1988).

12. A. Jones. "The development of megavoltage X-ray therapy at St. Bartholomew's Hospital". Br. J. Radiol., **22** (suppl), 3–10, (1988).

13. G. Failla, *An objective method for the administration of X-rays*, Acta Radiologica, **4**, 85–128, 1925.

14. Kerst, D. W. (1941). "The Acceleration of Electrons by Magnetic Induction". *Physical Review* **60**: 47–53.

15. T. P. Wangler. *RF Linear Accelerators* (Wiley-VCH, Weinheim, 2008).

16. H. E. Johns and J. R. Cunningham. "A precision cobalt 60 unit for fixed field and rotation therapy", Am. J. Roentgenol. Radium Therapy Nuclear Med, **81**, 4–12, (1959).

17. T. Kitabatake and S. Takahashi. "Conformation Radiotherapy by Means of 6 MeV Linear Accelerator", Tohoku J. exp. Med., **94**, 37–43, (1968).

18. C. X. Yu, C. J. Amies, and M. Svatos, "Planning and delivery of intensity-modulated radiation therapy", *Med. Phys*. **35**(12), 5233–5241, (2008).

19. D. Verellen, M. De Ridder, N. Linthout, *et al*. Innovations in image-guided radiotherapy. *Nature Reviews Cancer* **7**, 949–960 (2007).

20. L. A. Dawson, D. A. Jaffray. Advances in Image-Guided Radiation Therapy. *Journal of Clinical Oncology* **25**(8) 938–946 (2007).

21. International Commission on Radiation Units and Measurements, ICRU Report 50: Prescribing, Recording and Reporting Photon Beam Therapy (ICRU, Bethesda, 1993).

22. A. F. Monti, A. Ostinelli, M. Frigerio, et al. "An ICRU 50 radiotherapy treatment chart," Radiother. and Oncol., **35**, 145, (1995).

23. International Commission on Radiation Units and Measurements, ICRU Report 62: Prescribing, Recording and Reporting Photon Beam Therapy (Supplement to ICRU Report 50) (ICRU, Bethesda, 1999).

24. M. van Herk. Errors and Margins in Radiotherapy. *Seminars in Radiation Oncology* **14**(1) 52–54 (2004).

25. E. Rietzel, S. J. Rosenthal, D. P. Gierga, *et al.* Moving targets: detection and tracking of internal organ motion for treatment planning and patient set-up. *Radiother. Oncol.* **73** S68–S72 (2004).

26. K. M. Langen, T. L. Jones, Organ motion and its management *Int. J. Radiation Oncology Biol. Phys.* **50**(1) 265–278 (2001).

27. S. Webb. Motion effects in (intensity modulate) radiation therapy: a review. *Physics in Medicine and Biology* **51** R403–R42 (2006).

28. J. Leong, "Use of digital fluoroscopy as an on-line verification device in radiation therapy", *Phys. Med. Biol.* **31**(9), 985−992 (1986).

29. J. Pouliot, A. Bani-Hashemi, J. Chen, M. Svatos, F. Ghelmansarai, M. Mitschke, M. Aubin, P. Xia, O. Morin, K. Bucci, M. Roach, P. Hernandez, Z. R. Zheng, D. Hristov, and L. Verhey, "Low-dose megavoltage cone-beam CT for radiation therapy", *Int. J. Radiat. Oncol.* **61**(2), 552−560 (2005).

30. O. Morin, A. Gillis, J. Chen, M. Aubin, M. K. Bucci, M. Roach, and J. Pouliot, "Megavoltage cone-beam CT: system description and clinical applications", *Med. Dosim.* **31**(1), 51−61 (2006).

31. V. N. Hansen, P. M. Evans, and W. Swindell, "The application of transit dosimetry to precision radiotherapy", *Med. Phys.* **23**(5), 713−721 (1996).

32. K. L. Pasma, B. J. Heijmen, M. Kroonwijk, and A. G. Visser, "Portal dose image (PDI) prediction for dosimetric treatment verification in radiotherapy. I. An algorithm for open beams", *Med. Phys.* **25**(6), 830−840 (1998).

33. D. A. Jaffray, D. G. Drake, M. Moreau, A. A. Martinez, and J. W. Wong "A radiographic and tomographic imaging system integrated into a medical linear accelerator for localization of bone and soft-tissue targets", *Int. J. Radiat. Oncol.* **45**(3), 773−789 (1999).

34. D. A. Jaffray, J. H. Siewerdsen, J. W. Wong, and A. A. Martinez, "Flat-panel cone-beam computed tomography for image-guided radiation therapy", *Int. J. Radiat. Oncol.* **53**(5), 1337−1349 (2002).

35. T. R. Mackie, "History of tomotherapy", *Phys. Med. Biol.* **51**, R427–R453 (2006).

36. T. R. Mackie, J. Kapatoes, K. Ruchala, W. G. Lu, C. Wu, G. Olivera, L. Forrest, W. Tome, J. Welsh, R. Jeraj, P. Harari, P. Reckwerdt, B. Paliwal, M. Ritter, H. Keller, J. Fowler, and M. Mehta, "Image guidance for precise conformal radiotherapy", *Int. J. Radiat. Oncol.* **56**(1), 89−105 (2003).

37. K. J. Ruchala, G. H. Olivera, E. A. Schloesser, and T. R. Mackie, "Megavoltage CT on a tomotherapy system", *Phys. Med. Biol.* **44**(10), 2597−2621 (1999).

38. K. M. Langen, S. L. Meeks, D. O. Poole, T. H. Wagner, T. R. Willoughby, P. A. Kupelian, K. J. Ruchala, J. Haimerl, and G. H. Olivera, "The use of megavoltage CT (MVCT) images for dose recomputations", *Phys. Med. Biol.* **50**(18), 4259−4276 (2005).

39. W. Kilby, J. R. Dooley, G. Kuduvalli, S. Sayeh, and C. R. Maurer Jr., "The CyberKnife^® Robotic Radiosurgery System in 2010", *Technology in Cancer Research and Treatment*, **9**(5), 433−452 (2010).

40. H. Shirato, S. Shimizu, K. Kitamura, T. Nishioka, K. Kagei, S. Hashimoto, H. Aoyama, T. Kunieda, N. Shinohara, H. Dosaka-Akita, K. Miyasaka, "Four-dimensional treatment planning and fluoroscopic real-time tumor tracking radiotherapy for moving tumor", *Int. J. Radiat. Oncol.* **48**(2), 435−442 (2000).

41. P. G Seiler, H. Blattman, S. Kirsch, R. K. Muench, and C. Schilling "A novel tracking technique for the continuous precise measurement of tumour position in conformal radio therapy", *Phys. Med. Biol.* **45**(9), N103−N110 (2000).

42. J. D. P. Hoisak, K. E. Sixel, R. Tirona, P. Cheung, and J. P. Pignol, "Correlation of lung tumour motion with surrogates of respiration", *Med. Phys.* **31**(6), 1759 (2004).

43. J. Lattanzi, S. McNeeley, W. Pinover, E. Horwitz, I. Das, T. E. Schultheiss, and G. E. Hanks, " A comparison of daily CT localization to a daily ultrasound-based system in prostate cancer", *Int. J. Radiat. Oncol.* **43**(4), 719−725 (1999).

44. J. F. Dempsey, D. Benoit, J. R. Fitzsimmons, et al. "A Device for Real time 3D Image-Guided IMRT", *Int. J. Radiat. Oncol. Biol. Phys.*, **63,** S202−S202, (2005).

45. J. F. Dempsey. An Image-Guided Device Providing 4D CINE MRI Simultaneous to Radiotherapy Delivery. *Journal of Radiotherapy in Practice* **5** 179 (2006).

46. B. Fallone, M. Carlone, B. Murray, S. Rathee, T. Stanescu, S. Steciw, K. Wachowicz, and C. Kirkby, "Development of a linac-MRI system for real-time ART", *Med. Phys.* 34, 2547 (2007).

47. Lagendijk, J.J.W., Raaymakers, B.W., Raaijmakers, A.J.E., et al. MRI/linac integration. *Radiotherapy and Oncology* **86** 25−29 (2008).

48. B. G. Fallone, B. Murray, S. Rathee, *et al.* "First MR images obtained during megavoltage photon irradiation from a prototype integrated linac-MR system", *Med. Phys.*, **36,** 2084−2088, (2009).

49. B. W. Raaymakers, J. J. W. Lagendijk, J. Overweg, et al. "Integrating a 1.5 T MRI scanner with a 6 MV accelerator: proof of concept", *Phys. Med. Biol.*, **54,** N229−237, (2009).

50. J. G. M. Kok, B. W. Raaymakers, J. J. W. Lagendijk, J. Overweg, C. H. W. de Graaff and K. J. Brown. "Installation of the 1.5 T MRI accelerator next to clinical accelerators: impact of the fringe field", *Phys. Med. Biol.*, **54,** N409−N415, (2009).

51. C. Kirkby, T. Stanescu, S. Rathee, M. Carlone, B. Murray, and B. G.Fallone, "Patient dosimetry for hybrid MRI-radiotherapy systems", Med. Phys. **35,** 1019–1027 (2008).

52. C. Kirkby, B. Murray, S. Rathee, and B. G.Fallone "Lung dosimetry in a linac-MRI radiotherapy unit with a longitudinal magnetic field", Med. Phys. **37,** 4722–4732 (2010).

53. A. J. Raaijmakers, B. W. Raaymakers, and J. J. Lagendijk, "Magnetic-field-induced dose effects in MR-guided radiotherapy systems: Dependence on the magnetic field strength", Phys. Med. Biol. **53,** 909–923 (2008).

54. A. J. Raaijmakers, B. W. Raaymakers, and J. J. Lagendijk, "Integrating a MRI scanner with a 6 MV radiotherapy accelerator: Dose increase at tissue-air interfaces in a lateral magnetic field due to returning electrons", Phys. Med. Biol. **50**, 1363–1376 (2005).

55. B. W. Raaymakers, A. J. Raaijmakers, A. N. Kotte, D. Jette, and J. J. Lagendijk, "Integrating a MRI scanner with a 6 MV radiotherapy accelerator: Dose deposition in a transverse magnetic field", Phys. Med. Biol. **49**, 4109–4118 (2004).

56. A. F. Bielajew, "The effect of strong longitudinal magnetic fields on dose deposition from electron and photon beams", Med. Phys. **20**, 1171–1179 (1993).

57. Y. Chen, A. F. Bielajew, D. W. Litzenberg, J. M. Moran, and F. D. Becchetti, "Magnetic confinement of electron and photon radiotherapy dose: A Monte Carlo simulation with a nonuniform longitudinal magnetic field", Med. Phys. **32**, 3810–3818 (2005).

58. D. W. Litzenberg, B. A. Fraass, D. L. McShan, T. W. O. O'Donnell, D. A. Roberts, F. D. Becchetti, A. F. Bielajew, and J. M. Moran, "An apparatus for applying strong longitudinal magnetic fields to clinical photon and electron beams", Phys. Med. Biol. **46**, 401 (2001).

59. A. J. E. Raaijmakers, B. W. Raaymakers, S. van der Meer, and J. J. W. Lagendijk, "Integrating a MRI scanner with a 6 MV radiotherapy accelerator: impact of the surface orientation on the entrance and exit dose due to the transverse magnetic fields", Phys. Med. Biol. **52**, 929–939 (2007).

60. B. M. Oborn, P. E. Metcalfe, M. J. Butson, A. B. Rosenfeld, "High resolution entry and exit Monte Carlo dose calculations from a linear accelerator 6 MV

beam under the influence of transverse magnetic fields", Med. Phys. **36**, 3549–3559 (2009).

61. B. M. Oborn, P. E. Metcalfe, M. J. Butson, A. B. Rosenfeld, "Monte Carlo characterization of skin doses in 6 MV transverse field MRI-linac systems: effect of field size, surface orientation, magnetic field strength, and exit bolus", Med. Phys. **37**, 5208–5216 (2010).

62. B. M. Oborn, P. E. Metcalfe, M. J. Butson, A. B. Rosenfeld, P. J. Keall, "Electron contamination modeling and skin dose in 6 MV longitudinal field MRIgRT: Impact of the MRI and MRI fringe field", Med. Phys. **39**, 874–890 (2012).

CHAPTER 2 : THEORY AND TECHNIQUES

2.1 COMPUTATIONAL ELECTROMAGNETICS

The strong uniform magnetic field required by magnetic resonance imaging (MRI) devices is primarily produced by large magnetized pole pieces or immense superconducting coil configurations. In addition, large magnetic yoke structures are commonly employed in MRI magnet assemblies to passively shield the fringe magnetic fields while enhancing the field strength in the imaging volume. The design of an MRI magnet to obtain acceptable field uniformity and a fringe field with rapid fall off requires accurate modeling of the magnetic fields generated by these sources. This can be achieved by means of numerical techniques that accurately solve governing equations of electromagnetism.

In this section the fundamental equations of electrodynamics and a brief summary of the Finite Element Method (FEM) to solve these equations is presented. For a more rigorous treatment of the FEM method the reader is referred to Ref. [1].

2.1.1 The Theory of Electrodynamics

Electromagnetic fields and their interactions with matter in the classical regime are described by Maxwell's equations:[2]

$$\nabla \cdot \vec{D} = \rho, \tag{2.1a}$$

$$\nabla \cdot \vec{B} = 0, \tag{2.1b}$$

$$\nabla \times \vec{E} = -\frac{\partial \vec{B}}{\partial t}, \tag{2.1c}$$

$$\nabla \times \vec{H} = \vec{J} + \frac{\partial \vec{D}}{\partial t}, \tag{2.1d}$$

where ρ and $\vec{J}$ are the charge and current density distributions, respectively, $\vec{E}$ is the electric field, $\vec{B}$ is the magnetic field, $\vec{D}$ is the electric displacement, and $\vec{H}$ is the auxiliary magnetic field. If the fields are directly generated by known charge and current configurations, then the electric and magnetic fields are explicitly given by the generalized form of Coulomb's law[2] and Biot-Savart law[2], respectively.

The interaction of electromagnetic fields with matter is well characterized through the force they exert on charged particles. The fundamental equation describing the force $\vec{F}$ acting on a particle with charge q and velocity $\vec{v}$ is known as the Lorentz force law:[3]

$$\vec{F} = q\left[\vec{E} + \left(\vec{v} \times \vec{B}\right)\right]. \tag{2.2}$$

The electric $(\vec{E})$ and magnetic $(\vec{B})$ fields are "microscopic" quantities since they interact with intrinsic electric charge or spin angular momentum possessed by subatomic constituents of matter. The polarization or alignment of atoms and molecules of bulk materials in the presence of these external fields can result in a

net macroscopic electric polarization $\vec{P}$ (the electric dipole moment per unit volume) or magnetization $\vec{M}$ (the magnetic dipole moment per unit volume). With these macroscopic quantities the bulk properties of matter are expressed in terms of the macroscopic fields $\vec{D}$ and $\vec{H}$:[2]

$$\vec{D} = \epsilon_0 \vec{E} + \vec{P}, \tag{2.3a}$$

$$\vec{H} = \frac{1}{\mu_0}\vec{B} - \vec{M}, \tag{2.3b}$$

where ϵ_0 and μ_0 are the permittivity and permeability of the free space, respectively. For isotropic linear media the following relationships hold,[2]

$$\vec{P} = \epsilon_0 \chi_e \vec{E}, \tag{2.4a}$$

$$\vec{M} = \chi_m \vec{H}, \tag{2.4b}$$

where the constants χ_e and χ_m are the electric and magnetic susceptibilities, respectively. From Eqs. (2.3) and (2.4) for isotropic linear media we can write

$$\vec{D} = \epsilon \vec{E}, \tag{2.5a}$$

$$\vec{B} = \mu \vec{H}, \tag{2.5b}$$

where $\epsilon = \epsilon_0(1 + \chi_e)$ and $\mu = \mu_0(1 + \chi_m)$ are the permittivity and permeability of the medium, respectively.

Although χ_e is always a positive quantity, $\chi_m > 0$ for paramagnetic materials, containing atoms or molecules with unpaired electrons, and $\chi_m < 0$ for

30

diamagnetic materials. In practice, the susceptibilities of most media are not constant and in general are dependent on the temperature, the frequency content of time varying external fields, or the strength of the applied field.

The magnetization $\vec{M}$ in a given volume V enclosed in a boundary S contributes an effective volume and surface current $\vec{J}_M$ and $\vec{K}_M$ given by[2]

$$\vec{J}_M = \nabla \times \vec{M}, \tag{2.6a}$$

$$\vec{K}_M = \vec{M} \times \hat{n}, \tag{2.6b}$$

where $\hat{n}$ is the outward normal unit vector on S. The resulting magnetic field is then given by the Biot-Savart law.[1]

In general, the calculation of the magnetic fields from the explicit integrals of the Biot-Savart law is extremely tedious, if not impossible. However, in regions absent of currents or time varying fields the scalar magnetic potential formulation of the auxiliary field $\vec{H}$ can be a promising approach. In this case Eq. (2.1d) reduces to Ampere's law:

$$\nabla \times \vec{H} = 0. \tag{2.7}$$

Therefore, by the Helmholtz theorem[4] $\vec{H}$ can be expressed as the gradient of a scalar magnetic potential Φ_m:

$$\vec{H} = -\nabla \Phi_m. \tag{2.8}$$

31

Combining Eqs. (2.1b), (2.5b), and (2.8) one obtains

$$-\nabla \cdot (\mu \nabla \Phi_m) = 0, \qquad (2.9)$$

which in the special case where μ is constant reduces to

$$\nabla^2 \Phi_m = 0. \qquad (2.10)$$

Similar equations can be obtained for the vector components of $\vec{H}$ by taking the divergence of Eq. (2.7), since the divergence of a curl is always zero,

$$\nabla^2 H_x = \nabla^2 H_y = \nabla^2 H_z = 0. \qquad (2.11)$$

Therefore ϕ_m, H_x, H_y, and H_z all satisfy the Laplace equation which can be solved by expanding in terms of the spherical harmonics and applying appropriate boundary conditions to obtain the coefficients.[1]

In general, the problem of solving Eq. (2.9) for the scalar magnetic potential is very complicated and requires numerical techniques such as the finite element method (FEM).

2.1.2 The Finite Element Method

The finite element method[5,6] (FEM) is a numerical technique for calculating approximate solutions to partial differential equations of the general form:

$$\hat{\mathcal{L}} \, \Phi(\vec{r}) = f(\vec{r}), \quad \vec{r} \in \Omega, \tag{2.17}$$

where $\hat{\mathcal{L}}$ is a differential operator defined on the domain Ω, f is the source function, and Φ is the unknown quantity. With the boundary conditions enforced on Ω the problem in Eq. (2.17) essentially becomes a boundary value problem and the FEM converts it into a set of linear equations through discretization of the continuous domain Ω.

In the first step of the FEM implementation, the continuous domain Ω is discretized into a finite number of N_Ω polytopal subdomains (elements), each denoted Ω^p ($p = 1,2,\dots,N_\Omega$). The resulting collection of elements is referred to as the finite element mesh. Triangular and tetrahedral elements are the most widely used polytopes in the discretization of two- and three-dimensional problems since they have been shown to effectively conform to complex geometries and yield the greatest solution accuracy.[5] The solution Φ is then approximated within each of the finite elements by an interpolating polynomial Φ^p of order n_Ω with unknown coefficients. The interpolating functions are then combined to form a trial function $\widetilde{\Phi}$ that serves as the approximate global solution:

$$\Phi(\vec{r}) \approx \widetilde{\Phi}(\vec{r}) = \sum_{p=1}^{N_\Omega} \Phi^p(\vec{r}), \quad \vec{r} = (x,y,z) \in \Omega. \tag{2.18}$$

33

Each interpolating polynomial contains all the mixed terms of the coordinate variables x, y, and z. Thus, for a polynomial of order n_Ω there is a total of $m_\Omega = (1/6)(n_\Omega + 1)(n_\Omega + 2)(n_\Omega + 3)$ terms.[5] Accordingly, in each subdomain Ω^p, m_Ω nodal points will be defined, with the ith node being located at (x_i, y_i, z_i). For tetrahedral subdomains, each node is labeled with four integers (a_1, a_2, a_3, a_4) that satisfy $a_1 + a_2 + a_3 + a_4 = n_\Omega$. For the ith node the integer labels are defined as

$$a_1 = n_\Omega L_1^p(x_i, y_i, z_i), \tag{2.19a}$$

$$a_2 = n_\Omega L_2^p(x_i, y_i, z_i), \tag{2.19b}$$

$$a_3 = n_\Omega L_3^p(x_i, y_i, z_i), \tag{2.19c}$$

$$a_4 = n_\Omega L_4^p(x_i, y_i, z_i). \tag{2.19d}$$

In these equations $L_k^p(x, y, z)$ is the volume coordinate of the point (x, y, z) with respect to the kth vertex of the element Ω^p, given by

$$L_k^p(x, y, z) = \frac{V_k^p(x, y, z)}{V^p}, \quad k = 1, 2, 3, 4, \tag{2.20}$$

where V^p is the volume of Ω^p and $V_k^p(x, y, z)$ is the volume of the tetrahedron formed by replacing the kth vertex of Ω^p with the point located at (x, y, z). For a tetrahedral element with $n_\Omega = 2$ the nodal labels determined from Eq. (2.19) are shown in Fig. 2.1.
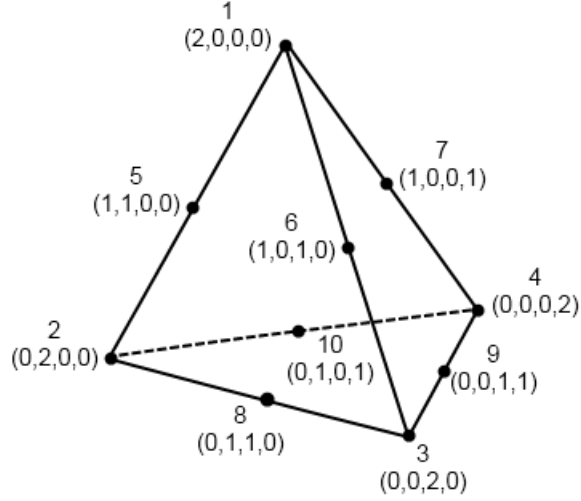
Figure 2.1: A second-order tetrahedral finite element showing local node numbers and volume coordinate indices defined in Eq. (2.19).

The interpolating polynomial $\Phi^p(\vec{r})$ can be expressed as

$$\Phi^p(x, y, z) = \sum_{i=1}^{m_\Omega} \Phi_i^p \, \mathfrak{S}_i^p(x, y, z). \tag{2.21}$$

The polynomial in Eq. (2.21) is constructed such that the coefficients Φ_i^p can be identified as the value of $\Phi^p(x, y, z)$ evaluated at (x_i, y_i, z_i), the location of the ith nodal point of subdomain Ω^p. Also, $\mathfrak{S}_i^p(x, y, z)$ denotes the finite element basis function, corresponding to the ith node, which is a polynomial of order n_Ω with the special property

$$\mathfrak{S}_i^p(x_j, y_j, z_j) = \delta_{ij}, \tag{2.22}$$

i.e. that its value is 1 when evaluated at the ith node, and 0 at any other nodal points. Specifically, the $\mathfrak{S}_i^p$'s are Lagrange basis functions and the subdomain Ω^p is referred to as a Lagrange finite element. These Lagrange basis functions are defined by the following generating formula in terms of the nodal labels and volume coordinates[6]

$$\mathfrak{S}_i^p(x, y, z) = \mathcal{G}_i^{a_1}(L_1^p)\, \mathcal{G}_i^{a_2}(L_2^p)\, \mathcal{G}_i^{a_3}(L_3^p)\, \mathcal{G}_i^{a_4}(L_4^p), \tag{2.23}$$

where $L_k^p = L_k^p(x, y, z)$ (the volume coordinates) and $\mathcal{G}_i^q(L_k^p)$ is the Lagrange interpolating polynomial of order q, for the ith node in Ω^p, defined as

$$\mathcal{G}_i^q(L_k^p) = \prod_{\substack{\ell=1 \\ \ell \neq i}}^{q} \frac{(L_k^p - L_{k\ell}^p)}{(L_{ki}^p - L_{k\ell}^p)}, \tag{2.24}$$

where $L_{ki}^p = L_k^p(x_i, y_i, z_i)$.

In the next step of the FEM the trial function $\widetilde{\Phi}$ is applied to the original boundary value problem of Eq. (2.17), leading to the generation and assembly of a large number of linear equations. The resulting system of equations can then be solved for the m_Ω unknown coefficients Φ_i^p of each of the N_Ω subdomains. This task can be accomplished utilizing the residual $\mathrm{F}(\Phi)$ defined as

$$\mathrm{F}(\Phi) = \hat{\mathcal{L}}\, \Phi - f. \tag{2.25}$$

With this definition the approximate solution of Eq. (2.17), $\widetilde{\Phi}$, will result in the least value of $\digamma(\widetilde{\Phi})$ at all points in Ω. At the core of the FEM, the attempt to minimize $\digamma(\widetilde{\Phi})$ is accomplished by means of Galerkin's method of weighted residual:[5,6]

$$R_i^p = \int_{\Omega^p} \mathfrak{S}_i^p \left(\hat{\mathcal{L}}\left[\widetilde{\Phi}(\vec{r})\right] - f(\vec{r}) \right) d\Omega' = 0, \quad \begin{cases} i = 1,2,\dots,m_\Omega \\ p = 1,2,\dots,N_\Omega \end{cases} \tag{2.26}$$

where the weighting functions $\mathfrak{S}_i^p$ are the finite element basis functions and $\widetilde{\Phi}(\vec{r})$ is expressed in terms of the unknowns Φ_i^p through Eqs. (2.18) and (2.21).

2.1.3 The FEM Applied to the Magnetostatics Problems of MRIs

Our group has been investigating the design and optimization of both permanent and superconducting magnets (see Ref [1]). This is accomplished by applying Maxwell's equations to the underlying structures and solving them by means of the FEM.

I. *MRI systems with a permanent magnet*

in magnetostatics problems with no free electrical current the following generalized constitutive relationship holds

$$\vec{B} = \mu_0 \left[\vec{H} + \vec{M}_{\text{ind}}(\vec{H}) + \vec{M}_r \right], \tag{2.27}$$

where $\vec{M}_r$ is the remanent magnetization vector corresponding to the remanent magnetic flux density $\vec{B} = \mu_0 \vec{M}_r$ of a permanent magnet when there is zero auxiliary magnetic field, and $\vec{M}_{\text{ind}}$ is the additional magnetization induced in the magnetic materials present in the system due to the presence of an auxiliary field. For isotropic linear media Eq. (2.4b) holds, $\vec{M}_{\text{ind}} = \chi_m \vec{H}$, and Eq. (2.27) reduces to

$$\vec{B} = \mu \vec{H} + \mu_0 \vec{M}_r, \tag{2.28}$$

where $\mu = \mu_0(1 + \chi_m)$ as before. Due to the absence of currents, $\vec{H}$ can be written in terms of a scalar magnetic potential

$$\vec{H} = -\nabla \Phi_m. \tag{2.29}$$

This result can be combined with Eqs. (2.1b) and (2.28) to obtain the second order partial differential equation:

$$-\nabla \cdot \left(\mu \nabla \Phi_m - \mu_0 \vec{M}_r \right) = 0, \tag{2.30}$$

By applying Galerkin's method of weighted residuals (Eq. (2.26)) to this equation one obtains

$$R_i^{\wp} = \int_{\Omega^{\wp}} \mathfrak{S}_i^{\wp} \left[\nabla \cdot \left(\mu \nabla \Phi_m - \mu_0 \overrightarrow{M}_r \right) \right] d\Omega' = 0, \tag{2.31}$$

where it is implied that $i = 1, 2, \ldots, m_{\Omega}$ and $\wp = 1, 2, \ldots, N_{\Omega}$.

II. *MRI systems with a superconducting magnet*

In magnetostatics problems with conductors carrying electrical current it is not possible to define $\overrightarrow{H}$ according to Eq. (2.29). In this case $\overrightarrow{H}$ can be separated into two components:

$$\overrightarrow{H} = \overrightarrow{H}_s + \overrightarrow{H}_m, \tag{2.32}$$

where $\overrightarrow{H}_s$ is the solenoidal component directly generated by the current distribution and $\overrightarrow{H}_m$ is the component due to any magnetic materials. Consequently, $\overrightarrow{H}_s$ can be calculated directly from the Biot-Savart law whereas $\overrightarrow{H}_m$ can be expressed as the gradient of a scalar magnetic potential:

$$\overrightarrow{H}_m = -\nabla \Phi_m. \tag{2.33}$$

Using the constitutive relationship in Eq. (2.28) with $\overrightarrow{M}_r = 0$ the magnetic field is given by

$$\overrightarrow{B} = \mu \left(-\nabla \Phi_m + \overrightarrow{H}_s \right). \tag{2.34}$$

Combining this equation with the divergence of $\overrightarrow{B}$ in Eq. (2.1b) yields

$$\nabla \cdot \left[\mu \left(-\nabla \Phi_m + \vec{H}_s \right) \right] = 0. \tag{2.35}$$

If the free currents are restricted to regions of uniform μ the second term in the above equation vanishes and we have

$$-\nabla \cdot (\mu \nabla \Phi_m) = 0. \tag{2.36}$$

Applying Galerkin's method of weighted residuals to this equation, we obtain

$$R_i^{\wp} = \int_{\Omega^{\wp}} \mathfrak{S}_i^{\wp} [-\nabla \cdot (\mu \nabla \Phi_m)] \, d\Omega', \tag{2.37}$$

The next step involves the replacement of Φ_m with the FEM approximation $\widetilde{\Phi}$ from Eqs. (2.18) and (2.21), and consequently the weighted residuals in Eqs. (2.31) and (2.37) can be expressed in matrix forms. Then, summing these matrices from all elements and setting the total residual to zero, in accordance with Galerkin's method, the final matrix equations will be obtained. For brevity, these steps are not shown in this thesis and the reader is referred to Ref [1] for more details.

2.2 MONTE CARLO SIMULATIONS TO MODEL PHOTON AND ELECTRON TRANSPORT

2.2.1 Introduction

In general, there are two methods to solve the problem of radiation transport in media: deterministic and stochastic. The widely used stochastic tool in the field of medical physics is Monte Carlo simulation where one employs the statistical nature of various interactions between photons and charged particles and the electrons, atoms, and nuclei of matter. In a Monte Carlo (MC) simulation random sampling of known probability distributions is used to determine the type and outcome of interaction events; simulating a large number of such events allows a statistical calculation of the dose deposited by incident photon or electron treatment beam in a given medium and geometry. Monte Carlo modeling is potentially the most accurate method to predict clinical dose distributions. This is particularly true for geometries that involve complex heterogeneities with densities that significantly deviate from unity. In such scenarios, such as small-field irradiation of lung (low density) or bone prosthesis (high density), electron disequilibrium is present and correction-based methods fail to predict the deviation from an in-water dose distribution. An alternative deterministic approach to Monte Carlo is to calculate dose distribution in media with complex heterogeneities from first principles, using the physics of photon and electron transport. Theoretically, it is possible to analytically solve the Boltzmann transport equation for the specific radiotherapy beam and medium conditions. However, there are so many variables affecting the resulting dose distribution that the transport equations are rendered almost impossible to solve without making many approximations in both formulating and solving the equations.

41

In Monte Carlo simulations, the process of following the motion and interactions of a particle is termed radiation transport since it mimics the way individual particles travel through a medium. Any daughter products produced by an incident particle are further transported through the geometry. The set of interactions initiated by an incident particle and complete transport of all the particles (source and its daughter products) is called a particle history. The unique history of an incident particle is determined by: (1) the geometry of the system and composition of the media, both of which are defined by the user in accord with the problem to be solved; (2) the initial position, direction, and energy of the incident particle, which are determined randomly within certain user-defined constraints; (3) random selection from the set of probability distributions governing the possible interactions of photons and electrons. Since the scored events are a result of stochastic processes, many (10^6 to 10^9) particle histories need to be simulated to determine the average behavior of a radiotherapy beam of particles with acceptable statistical precision.

2.2.2 Photon Transport

At any instant during a photon history the position, direction, and energy of the photon and secondary electrons it sets in motion are stored on a stack of variables. Then each particle is transported to its next position through a *step*, after which the variables on the stack are updated. The sequences of steps constituting a photon history are determined from the following key factors:

1) *Distance to the next interaction.* In a photon step, the particle is transported from its current position for a random distance. The probability of selecting a particular distance, x, is determined by the mean free path,

$$x = -\frac{\ln(\eta)}{\Sigma_{\text{total}}},$$

(2.38)

where η is a random number uniformly distributed between 0 and 1 and Σ_{total} is the total cross-section, which is related to the probability of a photon interaction occurring and depends on the current photon energy and the medium in which the photon currently resides.

2) *Type of interaction.* After a step is completed, a decision is made as to which type of interaction is to take place at the end of the step. The interaction type is chosen randomly from pre-generated probability distributions of photon interaction processes that depend on the current photon energy and medium composition. There are three main processes through which photons interact with a medium:

Compton scattering occurs when a photon of energy $h\nu$ collides with a "free" electron and transfers some of its energy, E_{tr}, to the electron. The photon is scattered with an energy $h\nu - E_{\text{tr}}$. The energy transferred, photon scattering angle, and initial direction of the recoil electron are determined by sampling from *Klein-Nishina* cross-section data.

43

The Photoelectric effect occurs when a photon of energy $h\nu$ is incident on an atom and loses all its energy in ejecting an orbital electron. The electron will carry a kinetic energy of $h\nu - E_b$, where E_b is the binding energy of the electron.

Pair production is a conversion of energy to mass where a photon with energy greater than 1.022 MeV loses this energy in production of an electron-positron pair. The positron eventually annihilates with an electron producing two 0.511 MeV gamma photons.

The type of interaction that occurs at the end of the step is determined by the fractional probability of each interaction. A new random number η is selected and if, for example, $\eta = \Sigma_{Compton} / \Sigma_{total}$ the Compton interaction is presumed to occur, otherwise one of the two other interactions is chosen.

3) *New angle and energy.* When the type of interaction has been chosen, further random numbers are generated and used to evaluate the energy and angular distribution of interaction products based on the respective probability distributions (cross-section tables) taking into account energy and the medium.

4) *New particles.* As a result of some interactions, such as pair production, new particles are created and/or set in motion. The position, direction and energy of these particles are added to the data stack.

2.2.3 Electron Transport and the Condensed-History Technique

The transport of charged particles, such as electrons and positrons, consumes most of the computing time in a Monte Carlo simulation since these particles interact with the medium at a much higher rate than photons. There are usually numerous short electron transport steps corresponding to each photon step. A typical megavoltage energy range electron, together with the secondary particles it sets in motion, undergoes in the order of 10^6 elastic and inelastic collisions until it is absorbed locally. Even with the use of supercomputers the simulation of all the individual collisions that electrons experience in the transport of a radiation beam becomes extremely time-consuming and hence impractical for routine clinical/research use. This shortcoming was first addressed by Berger through the condensed-history technique (CHT).[7] The CHT is based on the fact that most electron interactions result in extremely small changes in energy (through collision and radiative energy losses) and/or direction (after undergoing Coulomb scattering). Therefore, it is reasonable to group many small change collisions and straight line segments between them into a single "step". As such, only the cumulative effect of all collisions within the step is taken into account, by sampling energy, direction, and position changes from appropriate probability distributions of "inelastic" and "multiple scattering" interactions; e.g. Bethe-Block slowing down theory[8-10] and Moliere[11,12] multiple scattering theory . The

CHT provides an approximation to the exact electron transport; however it is mathematically proven that the CHT implementation converges to the correct result in the limit of small step sizes.[13]

A procedure used by the EGSnrc Monte Carlo codes to account for the large energy loss events that occur due to the production of delta rays and Bremsstrahlung is as follows: The threshold for discrete collision and radiative energy losses are controlled by two user-defined parameters AE and AP, respectively. Decreasing these parameters will increase the number of discrete interactions modeled, hence increasing the computation time. Collision energy losses below the energy $\Delta = AE - 0.511\,\text{MeV}$ and radiative energy losses below $AP\,\text{MeV}$ are characterized by the restricted total stopping power $(dE/dS)_{\Delta,AP}$. After a step length s, an electron with initial energy E_0 will have energy

$$E_1 = E_0 - s\left(\frac{dE}{dS}\right)_{\Delta,AP} - E_\delta - E_\gamma, \tag{2.39}$$

where the total energy of delta rays (E_δ) and Bremsstrahlung photons (E_γ) will decrease with increases in AE and AP, respectively. Energy deposited in the step is simply

$$E_{\text{dep}} = s\left(\frac{dE}{dS}\right)_{\Delta,AP}, \tag{2.40}$$

since the delta ray and Bremsstrahlung energies will be deposited elsewhere.

2.2.4 Implementation of the Electromagnetic Fields into the Monte Carlo Simulations

To account for the effects of external electromagnetic fields on the charged-particle transport one needs to incorporate the electric and magnetic fields into the condensed-history Monte Carlo simulations. This was first implemented by Alex F. Bielajew,[14] who superimposed the transport in the external fields and in vacuum upon "field-free" charged particle transport, based on certain approximations. All dosimetric simulations in the work of this thesis are performed using EGSnrc Monte Carlo codes that are based on a "condensed history" treatment. In this chapter, a summary of the original work of Alex F. Bielajew[14] that implements static external electromagnetic vector fields into the EGSnrc Monte Carlo codes is presented. In the first section we establish the equations that govern external-field transport of charged particles in vacuum. We then discuss what approximations are necessary to minimize the error when the vacuum transport equations are tacked on to the field-free transport. In the last part we present the details of implementing external-field transport equations into a Monte Carlo code.

2.2.4.1 Equations of Motion of a Charged Particle in Vacuum

When a charged particle moves in electric $\vec{E}$ and magnetic $\vec{B}$ fields, its momentum $\vec{p}$ changes with time according to the Lorentz force equation[3]

$$\frac{d\vec{p}}{dt} = q(\vec{E} + \vec{v} \times \vec{B}), \tag{2.41}$$

where t is the time, q is the charge of the particle, and $\vec{v}$ is the velocity. Using the relativistic factors $\vec{\beta} = \vec{v}/c$ (where c is the speed of light) and $\gamma = (1 - \vec{\beta} \cdot \vec{\beta})^{-1/2}$, one can express the time dt in terms of the differential path length ds through $ds = (ds/dt)dt = vdt = (c\beta)dt$ and the momentum as $\vec{p} = m\vec{v} = mc\vec{\beta} = \gamma m_0 c\vec{\beta}$ (where m_0 is the rest mass of the particle). Then, Eq. (2.41) can be written as

$$\frac{d(\gamma\vec{\beta})}{ds} = \frac{q}{m_0 c^2 \beta}(\vec{E} + c\vec{\beta} \times \vec{B}). \tag{2.42}$$

Expanding the differential operator on the left-hand side of Eq. (2.42) as $d(\gamma\vec{\beta}) = \gamma d\vec{\beta} + \vec{\beta}d\gamma$ and expressing $d\gamma = \gamma^3(\vec{\beta}.d\vec{\beta})$, Eq. (2.42) reduces to

$$\gamma\frac{d\vec{\beta}}{ds} + \gamma^3\frac{\vec{\beta}(\vec{\beta}.d\vec{\beta})}{ds} = \frac{q}{m_0 c^2 \beta}(\vec{E} + c\vec{\beta} \times \vec{B}). \tag{2.43}$$

If one takes the inner product of both sides of the above equation with $\vec{\beta}$ the second term on the right-hand side vanishes and one obtains

$$\gamma^3 \frac{(\vec{\beta}.d\vec{\beta})}{ds} = \frac{q}{m_0 c^2 \beta} (\vec{E}.\vec{\beta}).$$ (2.44)

Substituting Eq. (2.44) into Eq. (2.43) yields

$$\frac{d\vec{\beta}}{ds} = \frac{q}{m_0 c^2 \beta \gamma} (\vec{E} - \vec{\beta}(\vec{E}.\vec{\beta}) + c\vec{\beta} \times \vec{B}).$$ (2.45)

This equation can be rewritten in terms of the unit direction vector of the charged particle, $\vec{u}$:

$$\frac{d\vec{u}}{ds} = \frac{q}{m_0 c^2 \beta^2 \gamma} (\vec{E} - \beta^2 \vec{u}(\vec{E}.\vec{u}) + c\beta\vec{u} \times \vec{B}).$$ (2.46)

Alternatively, we can express Eq. (2.45) in units of force,

$$\frac{d\vec{p}}{dt} = q(\vec{E} - \vec{\beta}(\vec{E}.\vec{\beta}) + \vec{v} \times \vec{B}).$$ (2.47)

We will use Eqs. (2.46) and (2.47) to incorporate external-field transport of charged particles into a Monte Carlo code.

2.2.4.2 Charged Particle Transport in a Medium

A charged particle moving in a medium with external electric and magnetic fields couples to the external fields and undergoes elastic (multiple scattering) and inelastic interactions. Assuming the medium is isotropic and homogeneous, the equation of motion takes the general form

$$\frac{d\vec{p}}{dt} = \vec{F}_{\text{ret}}\big(E(t)\big) + \vec{F}_{\text{ms}}\big(E(t)\big) + \vec{F}_{\text{em}}\big(\vec{x}(t), E(t), \vec{u}(t)\big), \qquad (2.48)$$

where $\vec{p}$ is the momentum, t is the time, $\vec{F}_{\text{ret}}$ is the force due to inelastic (retarding) interactions, $\vec{F}_{\text{ms}}$ is the force due to elastic (multiple scattering) interactions, $\vec{F}_{\text{em}}$ is the electromagnetic force. In this equation $E(t)$, $\vec{x}(t)$, and $\vec{u}(t) = \vec{v}(t)/|\vec{v}(t)|$ are the energy, position vector, and the unit direction vector of the charged particle respectively. Integrating Eq. (2.48) implicitly, one obtains

$$\vec{v} = \vec{v}_0 + \frac{1}{m_0 \gamma(E)} \int_0^t dt' \; \big\{ \vec{F}_{\text{ret}}\big(E(t')\big) + \vec{F}_{\text{ms}}\big(E(t')\big)$$
$$+ \vec{F}_{\text{em}}\big(\vec{x}(t'), E(t'), \vec{u}(t')\big) \big\}, \qquad (2.49\text{a})$$

$$\vec{x} = \vec{x}_0 + \vec{v}_0 t + \int_0^t dt'' \; \vec{v}(t''). \qquad (2.49\text{b})$$

These equations are quite complicated and the interplay among different forces makes it very difficult to solve them directly: The main inelastic processes $(\vec{F}_{\text{ret}})$ are electron-electron interactions and Bremsstrahlung photon creation in the nuclear field which alter the energy, $E(t)$, and consequently the magnitude of the velocity, v. There is some deflection involved in inelastic processes as well, but it is dominated by multiple scattering. Therefore $\vec{F}_{\text{ret}}$ couples to $\vec{F}_{\text{ms}}$ and $\vec{F}_{\text{em}}$ since they all depend on the energy. Multiple scattering $(\vec{F}_{\text{ms}})$ mainly accounts for deflections caused by the nuclei of the medium; hence it changes the direction of the velocity, $\vec{u}(t)$. The energy lost to the recoiled nucleus is quite small and can

be ignored. Consequently, $\vec{F}_{ms}$ couples to $\vec{F}_{em}$ since the Lorentz force depends on the direction of motion of the particle. In general, the interaction of the charged particles with the electric and magnetic fields, $\vec{F}_{em}$, depends on the energy, position, and direction of the velocity. Since $\vec{F}_{em}$ can alter both the magnitude and direction of the velocity, $\vec{v}$, it couples to both $\vec{F}_{ret}$ and $\vec{F}_{ms}$. Furthermore, the mass changes with the energy change due to the relativistic effects, bringing a factor of $1/m_0 \gamma(E)$ outside the integral in Eq. (2.49a). Therefore, it is essential to decouple $\vec{F}_{em}$ from forces due to inelastic and multiple scattering interactions.

During the condensed-history transport step the trajectory of the particle and the exact forms of $\vec{F}_{ret}$ and $\vec{F}_{ms}$ are not known. Therefore, we need to make use of the already existing statistical treatments of $\vec{F}_{ret}$ and $\vec{F}_{ms}$ (e.g. Bethe-Block slowing down theory[8-10] and Moliere[11,12] multiple scattering theory) by decoupling the Lorentz force from $\vec{F}_{ret}$ and $\vec{F}_{ms}$. Furthermore, if the external fields are different for different possible particle trajectories, the problem of performing integral Eq. (2.49a) remains unsolvable. Thus, we must demand that *the step size of a condensed-history transport is small enough such that the change in the external electric and magnetic fields are sufficiently small over the course of the step*. Under this approximation Eq. (2.49a) reduces to

$$\vec{v} = \vec{v}_0 + \frac{1}{m_0 \gamma(E)} \int_0^t dt' \; \{\langle \vec{F}_{\text{ret}}(E(t')) \rangle + \langle \vec{F}_{\text{ms}}(E(t')) \rangle$$

$$+ \vec{F}_{\text{em}}(\vec{x}_0, E(t'), \vec{u}(t'))\}, \tag{2.50}$$

where $\vec{x}_0$ denotes particle's position at the beginning of the transport step and $\langle \vec{F} \rangle$'s denote the statistical treatment of inelastic and multiple scattering processes.

We further simplify the problem by making the approximation that *the change in the particle's energy during the transport step is small*, and then Eq. (2.50) becomes

$$\vec{v} = \vec{v}_0 + \frac{1}{m_0 \gamma(E_0)} \Big\{ \langle \vec{F}_{\text{ret}}(E_0) \rangle t + \langle \vec{F}_{\text{ms}}(E_0) \rangle t$$

$$+ \int_0^t dt' \; \vec{F}_{\text{em}}(\vec{x}_0, E_0, \vec{u}(t')) \Big\}, \tag{2.51}$$

where E_0 is the energy of the charged particle evaluated at the beginning of the transport step.

Finally, we make the approximation that by sufficiently reducing the step size in the condensed-history algorithm *the angle of the unit direction vector $\vec{u}(t)$ does not change much over the course of the step*. This approximation is valid for most of the charged-particle steps but it breaks down occasionally when single nucleus-electron interactions produce large-angle scatterings. It is known that multiple

scattering is dominated by small-angle events with only relatively few large-angle ones[7], thus we can apply this approximation to Eq. (2.51) with little error:

$$\vec{v} = \vec{v}_0 + \frac{t}{m_0 \gamma(E_0)} \{ \langle \vec{F}_{\text{ret}}(E_0) \rangle + \langle \vec{F}_{\text{ms}}(E_0) \rangle$$

$$+ \vec{F}_{\text{em}}(\vec{x}_0, E_0, \vec{u}_0) \},$$

(2.52)

where $\vec{u}_0$ is the direction vector evaluated at the beginning of the transport step. All forces are now decoupled in Eq. (2.52) and the assumptions we have made guarantees that the Lorentz force does not perturb the "external force-free" trajectory too much.

In order to implement the equations into the Monte Carlo simulations we will express the time in terms of the total path length of the transport step s:

$$t = \int_0^s \frac{ds}{v}.$$

(2.53)

This relation, to 1$^{\text{st}}$-order, can be written as

$$t = \frac{s}{v_0} \left(1 + \frac{\Delta v(E_0)}{v_0} \right),$$

(2.54)

where $\Delta v(E_0) = v_0 - v(E_0)$ accounts for the energy loss over the course of the step. Using the first term in the expression for the time, i.e. $t = s/v_0$, we can recast Eq. (2.52), to 1$^{\text{st}}$-order, as

53

$$\Delta v(E_0) = -\frac{s}{m_0 \gamma(E_0) v_0} \vec{u}_0 \cdot \{\langle \vec{F}_{\mathrm{ret}}(E_0) \rangle + \langle \vec{F}_{\mathrm{ms}}(E_0) \rangle$$

$$+ \vec{F}_{\mathrm{em}}(\vec{x}_0, E_0, \vec{u}_0)\}, \tag{2.55}$$

with $\vec{u}_0 = \vec{v}_0/v_0$ being the direction vector at the start of the particle transport step. It follows from Eq. (2.55) that the change in the direction vector $\Delta\vec{u} = \vec{u} - \vec{u}_0 = \Delta\vec{v}/v_0$ takes the form

$$\Delta\vec{u} = \frac{s}{m_0 \gamma(E_0) v_0^2} \{\langle \vec{F}_{\perp,\mathrm{ret}}(E_0) \rangle + \langle \vec{F}_{\perp,\mathrm{ms}}(E_0) \rangle$$

$$+ \vec{F}_{\perp,\mathrm{em}}(\vec{x}_0, E_0, \vec{u}_0)\}, \tag{2.56}$$

where $\vec{F}_\perp$'s are the components of the forces in the direction perpendicular to the unit direction vector $\vec{u}_0$. Equation (2.55) is one of the fundamental equations that we will use to incorporate electromagnetic interactions into the "external force-free" condensed-history Monte-Carlo algorithm.

Next, we will make use of Eq. (2.54) in Eq. (2.49b) to calculate the change in the position of the charged particle. Again, to 1$^\text{st}$-order, we can replace the time t with s/v_0 and the 2$^\text{nd}$ term in Eq. (2.49b) becomes $\vec{v}_0 t = \vec{v}_0 s/v_0 = \vec{u}_0 s$. The third term in Eq. (2.49b) can be evaluated by using both terms in Eq. (2.54) to replace the time; from Eq. (2.54) we can write

$$dt = -\frac{s}{v_0^2} dv, \tag{2.57}$$

and then

$$\int_0^t dt''\ \vec{v}(t'') = \int_v^{v_0} dv'\overrightarrow{v'}\left[-\frac{s}{v_0^2}\right] = \frac{s}{2v_0^2}(v^2\vec{u} - v_0^2\vec{u}_0)$$

$$= \frac{s}{2}\left(\frac{v^2}{v_0^2}\vec{u} - \vec{u}_0\right) \approx \frac{s}{2}\Delta\vec{u}.$$

(2.58)

Finally, Eq. (2.49b) reduces to

$$\vec{x} = \vec{x}_0 + \vec{u}_0 s + \frac{s}{2}\Delta\vec{u}.$$

(2.59)

The deflection, $\Delta\vec{u}$, contains the three decoupled forces (Eq. (2.56)), allowing us to rewrite Eq. (2.59) in a slightly different form

$$\vec{x} = \vec{x}_0 + \vec{u}_0 s + \vec{\epsilon}^{(1)}_{\perp,\text{ret+ms}} + \vec{\epsilon}^{(1)}_{\perp,\text{em}},$$

(2.60)

where $\vec{\epsilon}^{(1)}_{\perp,\text{ret+ms}}$ is the 1$^{\text{st}}$-order perturbation of the trajectory due to inelastic slowing down plus multiple scattering, and $\vec{\epsilon}^{(1)}_{\perp,\text{em}}$ is the 1$^{\text{st}}$-order perturbation due to the deflection and energy change in the external electric and magnetic fields. Since $\vec{\epsilon}^{(1)}$'s are decoupled we can calculate $\vec{\epsilon}^{(1)}_{\perp,\text{ret+ms}}$ using the condensed-history algorithm in the absence of the external fields, and $\vec{\epsilon}^{(1)}_{\perp,\text{em}}$ by transporting charged particles in vacuum. Note that to 1$^{\text{st}}$-order the deflections are transverse to the initial trajectory (Eqs. (2.55) and (2.56)).

2.2.4.3 Application to Monte Carlo

In the condensed-history treatment of charged particle Monte Carlo transport, aside from those interactions that are considered explicitly, the interactions are grouped together and treated by theories which consider the medium to be a homogeneous, bulk medium. To be consistent with the condensed-history approach the macroscopic fields, $\vec{D}$ and $\vec{H}$, must be used; rather than the microscopic fields, $\vec{E}$ and $\vec{B}$. The microscopic domain refers to the electric and magnetic fields that are experienced by individual electrons and nuclei of atoms in the medium where the transport takes place. In contrast, macroscopic fields describe the bulk properties of the materials present.

At the start of a charged-particle transport step in the presence of external fields, all physical quantities are known: the position, $\vec{x}_0$, the unit direction vector, $\vec{u}_0$, the energy, E_0, (and hence the speed, v_0, or $\beta_0 = v_0/c$), the macroscopic electric, $\vec{D}_0$, and magnetic, $\vec{H}_0$, fields at $\vec{x}_0$. We will use the results of the previous sections to find the final position, $\vec{x}_f$, unit direction vector, $\vec{u}_f$, and energy, E_f, of the particle after the transport step. From Eq. (2.47) the transverse force on the charged particle, at the start of the transport step, due to external electric and magnetic fields can be written as

$$\vec{F}_{\perp,\text{em}}(\vec{x}_0, E_0, \vec{u}_0) = q\left(\vec{D}_0 - \beta_0^2\, \vec{u}_0\left(\vec{u}_0 \cdot \vec{D}_0\right) + \vec{v}_0 \times \vec{H}_0\right). \tag{2.61}$$

Using the above equation and Eq. (2.56), the unit direction vector at the end of the transport step is,

$$\vec{u}_f = \vec{u}_0 + \Delta\vec{u}_{ms,ret} + \Delta\vec{u}_{em}, \tag{2.62}$$

where the deflection of the charged particle due to multiple scattering and inelastic collisions is:

$$\Delta\vec{u}_{ms,ret} = \frac{s}{m_0\gamma(E_0)v_0^2}\{\langle\vec{F}_{\perp,ret}(E_0)\rangle + \langle\vec{F}_{\perp,ms}(E_0)\rangle\}, \tag{2.63}$$

and the deflection due to the external electric and magnetic fields is:

$$\Delta\vec{u}_{em} = \frac{qs}{m_0\gamma(E_0)v_0^2}\left(\vec{D}_0 - \beta_0^2\,\vec{u}_0(\vec{u}_0\,.\,\vec{D}_0) + \vec{v}_0\times\vec{H}_0\right). \tag{2.64}$$

At this point we need to make sure that the new direction vector is properly normalized, i.e. $|\vec{u}_f| = 1$. To this end, we normalize $\vec{u}_f$ after the transport is accomplished using,

$$\vec{u}_f' = \frac{\vec{u}_f}{\sqrt{1 + |\Delta\vec{u}_{ms,ret}|^2 + 2\Delta\vec{u}_{ms,ret}\,.\,\Delta\vec{u}_{em} + |\Delta\vec{u}_{em}|^2}}. \tag{2.65}$$

The position of the particle at the end of the step can be determined from Eqs. (2.59) and (2.62)-(2.64):

$$\vec{x}_f = \vec{x}_0 + \vec{u}_0 s + \frac{s}{2}\left(\Delta\vec{u}_{ms,ret} + \Delta\vec{u}_{em}\right). \tag{2.66}$$

57

Finally, we calculate the energy of the particle at the end of the transport step using,

$$E_f = E_0 - \Delta E_{ret} + q\vec{D}_0 \cdot (\vec{x}_f - \vec{x}_0). \tag{2.67}$$

In this equation ΔE_{ret} is the energy loss due to inelastic collisions:

$$\Delta E_{ret} = \int_0^s ds' \left| \frac{dE}{ds'} \right|, \tag{2.68}$$

where $|dE/ds'|$ is the stopping power.

To reiterate, the accuracy of Eqs. (2.62), (2.66) and (2.67) rely on the validity of 1st-order approximations that requires that the following constraints are met:

1. The fields should not change very much over the transport step,

$$\frac{\left| \vec{D}(\vec{x}_f) - \vec{D}(\vec{x}_0) \right|}{\left| \vec{D}(\vec{x}_0) \right|} \ll 1, \tag{2.69a}$$

$$\frac{\left| \vec{H}(\vec{x}_f) - \vec{H}(\vec{x}_0) \right|}{\left| \vec{H}(\vec{x}_0) \right|} \ll 1. \tag{2.69b}$$

2. The energy should not change very much over the transport step,

$$\frac{\Delta E_{ret}}{E_{0,kinetic}} \ll 1, \tag{2.70a}$$

$$\frac{\left| \Delta E_{em} \right|}{E_{0,kinetic}} \ll 1. \tag{2.70b}$$

58

3. The direction should not change very much over the transport step,

$$\left|\Delta\vec{u}_{\text{ms,ret}}\right| \ll 1, \tag{2.71a}$$

$$\left|\Delta\vec{u}_{\text{em}}\right| \ll 1. \tag{2.71b}$$

All of these constraints can be satisfied by using a small charged-particle step size, with the exception of the one expressed in Eq. (2.71a), which will be violated for large-angle, single-event Rutherford scattering. Such events occur in high-Z media, which produce more large-angle scattering, (not sure quite what this is saying – delete if not necessary). Since large-angle events occur infrequently the error introduced should generally be insignificant.

As in Ref. [14], Bielajew summarized the implementation of his algorithm for electron transport in media in the presence of external electric and magnetic fields by the following six steps: :

1. Choose a total path length for the step, s, that satisfies the constraints expressed in Eqs. $(2.69) - (2.71)$.
2. Evaluate the inelastic and elastic-scattering interactions, $\langle\vec{F}_{\perp,\text{ret}}(E_0)\rangle$ and $\langle\vec{F}_{\perp,\text{ms}}(E_0)\rangle$, using any slowing-down and multiple-scattering theory, then calculate $\vec{u}_f$ using Eqs. $(2.62) - (2.64)$.
3. Transport the charged particle according to Eq. (2.66).
4. Normalize the direction vector, $\vec{u}_f$, using Eq. (2.65).
5. Calculate the new energy according to Eqs. (2.67) and (2.68).
6. Repeat.

59

2.3 REFERENCES

1. T. Tadic. "Magnet design and optimization for an integrated linac-MRI system," Ph.D. thesis, (University of Alberta, 2012).

2. D. J. Griffiths, Introduction to Electrodynamics, 3rd ed. (Prentice Hall, Upper Saddle River, 1999).

3. J. D. Jackson, Classical Electrodynamics, 3rd ed. (Wiley, New York, 1999).

4. G. B. Arfken and H. J. Weber, Mathematical Methods for Physicists, 6th ed. (Elsevier, Burlington, 2005).

5. J. Jin, The Finite Element Method in Electromagnetics, 2nd ed. (Wiley, New York, 2002).

6. O. C. Zienkiewicz, R. L. Taylor, and J. Z. Zhu, The Finite Element Method: Its Basis and Fundamentals, 6th ed. (Elsevier, Oxford, 2005).

7. M. J. Berger, "Monte Carlo calculation of the penetration and diffusion of fast charged particles." In *Methods in Computational Phsyics, Volume I Statistical Physics*. B. alter, S. Fernbach, M. Rotenberg (Eds.). (New York: Academic Press), pp. 135−215, 1963.

8. H. A. Bethe, "Theory of passage of swift corpuscular rays through matter", Ann. Physik. **5**, 325 (1930).

9. H. A. Bethe, "Scattering of Electrons", Z. Phys. **76**, 293 (1932).

10. F. Block, "Stopping power of atoms with several electrons", Z. Phys. **81**, 363 (1993).

11. G. Z. Moliere, "Theorie der Streuung Schneller Geladener Teilchen. I. Einzel-streuung am Abgeschirmten Coulom-Feld", Z. Naturforsch. **A2**, 133 (1947).

12. G. Z. Moliere, "Theorie der Streuung schneller geladener Teilchen II Mehrfach-und Vielfachstreuung", Z. Naturforsch. **A3**, 78 (1948).

13. E. W. Larsen, "A theoretical derivation of the condensed history algorithm." Ann. Nucl. Energy **19**, 701−714 (1992).

14. A.F. Bielajew, "Electron Transport in $\vec{E}$ and $\vec{B}$ Fields," in "Monte Carlo Transport of Electrons and Photons Below 50 MeV", eds. T.M. Jenkins, W.R. Nelson, A. Rindi, A.E. Nahum and D.W.O. Rogers, (Plenum Press) 421–434 (1989).

CHAPTER 3 : MATERIALS AND METHODS

3.1 REALISTIC 3D MAGNETIC FIELDS

Commercially available Finite Element Method (FEM) software packages, Comsol Multiphysics[1] and Opera-3D[2], were used to calculate the realistic 3D magnetic fields for the different MRI systems considered below. Corresponding measurements of the magnetic fields were not performed since the systems modeled are not yet ready for experimentation. However, these FEM packages have been benchmarked extensively, previously. Various groups worldwide have compared calculated magnetic field vectors for other magnet designs using these software packages with experimental measurements.[3-5]

3.1.1 Generic Yoked "Helmholtz-Pair" MRI System

To investigate the effects of realistic magnetic fields on patient skin dose, we first simulated a generic Helmholtz coil assembly. The magnetic fields from the "Helmholtz-pair" (Helmholtz) coils were calculated by using Comsol Multiphysics.[1] Each superconducting coil in the model had with inner radius of 40 cm and a rectangular cross-section of 10 x 5 cm^2. Current densities of 5.975 and 2.988 kA/cm^2, which can be achieved by using currently available superconducting materials such as (NbTi) and (MgB_2)[6], were used to produce magnetic field strengths of 1.0 and 0.5 T, respectively. The 0.5 T Helmholtz MRI

is representative of a commercially available system. Although a 1.0 T Helmholtz MRI is currently not commercially available, it is used to facilitate comparison with the magnetic field models from Oborn *et al.* that were based on a 1.0 T main magnetic field. For each system modeled, a Helmholtz configuration was created by placing one coil on each side of the perceived imaging volume. The pair of coils was held by a simple yoke consisting of a pair of AISI 1020 carbon steel[7] disks (20 cm thick, 75 cm radius). The two sides of the magnet were separated by four steel posts (radius of 7.5 cm and 52 cm in length). In order to simulate a longitudinal RBP geometry, a 32.5 cm radius hole is made in each disk to ensure an unobstructed path for the X-ray beam from the linac. To further investigate the effect of a yoke structure on the MRI fringe fields, a 1.0 T Helmholtz-pair system without a yoke was also simulated. The FEM simulations used quadratic vector basis functions with tetrahedral finite elements that were optimized through Delaunay triangulation.[1] A Neumann or natural boundary condition was specified at the model's external boundaries.[1] The magnetic fields were solved through a direct solver. Further details regarding this simulation can be found in Ref. [1].

3.1.2 Mid-Field (0.56 T) Yoked Bi-Planar Superconducting (CCI) Magnet Assembly

Opera-3D[2] was used to calculate the complete 3D magnetic field generated by the realistic linac-MRI systems illustrated in Fig. 3.1. Details of the modeling

procedure and magnetic field analysis of this system have been reported by Tadic and Fallone[8], the important aspects of which are reviewed below.
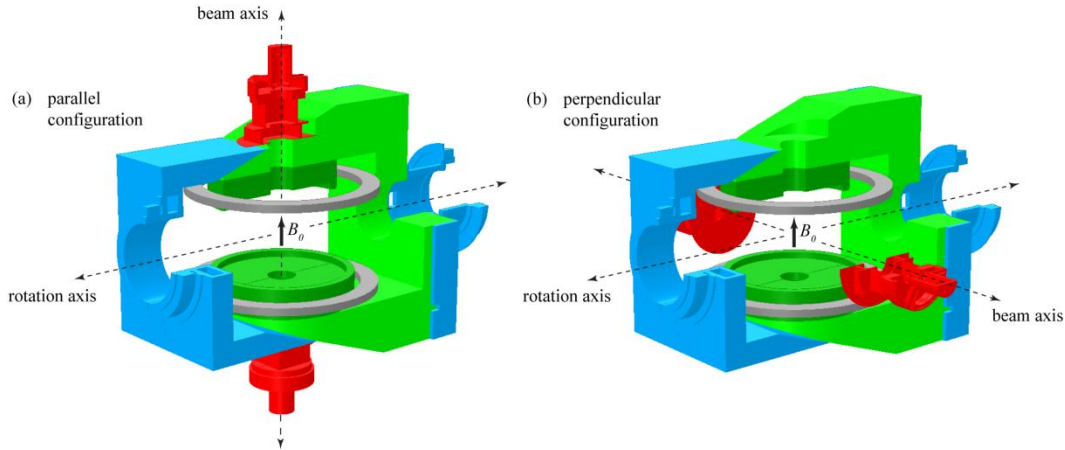
Figure 3.1: Partial sections of the three-dimensional linac-MRI geometries simulated with the finite element method. Both (a) parallel (longitudinal) and (b) perpendicular (transverse) configurations are illustrated, with the biplanar magnet assembly shown in green, the superconducting coil in grey, the treatment assembly in red, and the gantry support link in blue. (Courtesy of Dr. Tony Tadic)

The linac-MR system consists of three principal magnetic components: a bi-planar superconducting MRI magnet assembly, a treatment machine assembly including the linac and associated components in the linac head, and a mechanical gantry link. The magnet assembly consists of a C-shaped yoke structure constructed from AISI 1020 plain carbon steel and a pair of magnetic pole pieces made of Armco magnetic steel. The magnetic pole pieces act to enhance the magnetic field strength in the imaging volume and can be appropriately shaped to improve the field homogeneity.[9, 10] This magnet assembly has a 60 cm pole-to-

pole separation, and a 24 cm diameter hole bored through the yoke and pole structures. A single large coil constructed from MgB_2 high-temperature superconducting material surrounds each of the pole pieces and acts as a magnetic source. These coils are of rectangular cross-section and possess a current density of 1.764 kA/cm^2.

The magnetic assembly surrounding the linac and the associated components is illustrated in Fig. 3.2. It is comprised of the passive magnetic linac shielding, the electron gun casing, the linac base, secondary collimator base, and the multileaf collimator (MLC) base, all of which were taken to be constructed from AISI 1020 steel.[8] Although the actual treatment assembly consists of many relatively small magnetic elements, the structures modeled for this study possess equivalent magnetic masses and approximate the true distribution of magnetic material, making simulation of the entire system practical.

Magnetic field simulations were performed with the treatment assembly in both parallel and perpendicular linac-MRI configurations, as depicted in Fig. 3.1. The treatment assemblies were positioned along the beam axis such that linac target to isocenter distances of 126 cm and 146 cm were obtained for the parallel and perpendicular configurations, respectively. The latter distance was necessarily increased to avoid physical interference of the MLC subassembly with the cryostat and pole structures of the MRI magnet.

65
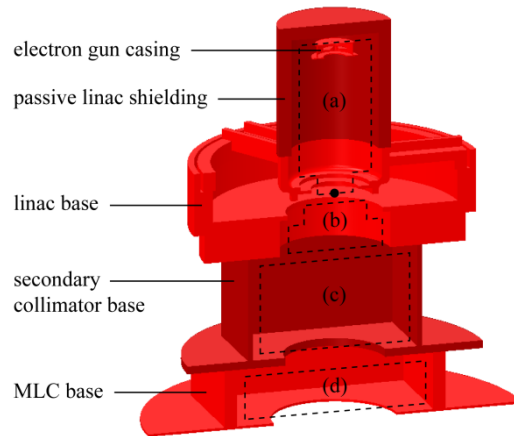
Figure 3.2: Partial section of the magnetic treatment assembly, including the electron gun casing, passive magnetic linac shielding, linac base, secondary collimator base, and MLC base. With reference to the Monte Carlo particle simulations, the dotted regions depict the approximate locations of (a) the electron gun and linac waveguide, (b) the primary collimator, flattening filter, and monitor chambers, (c) the movable secondary collimator jaws, and (d) the movable MLC leaves. (Courtesy of Dr. Tony Tadic)

The mechanical gantry link, as shown in Fig. 3.1, was also modeled as being composed of AISI 1020 steel. This structure provides increased mechanical support of the linac-MRI system and the necessary components for mating the integrated system with a rotating gantry. Due to symmetry in the magnet assembly and associated magnetic fields, only one quarter of both linac-MRI geometries was modeled within a large rectangular domain extending 15 m from isocenter along each Cartesian axis. The modeled 3D space was divided into approximately 3.8×10^6 iso-parametric tetrahedral, quadratic Lagrange elements, and the complete 3D magnetic fields were obtained with the Tosca module of Opera-3D.

3.2 MONTE CARLO SIMULATIONS

All Monte Carlo simulations were performed using EGSnrc and BEAMnrc radiation transport codes with algorithms implemented to account for the magnetic field deflection of charged particles.[11-17] The simulations were run on the Western Canadian Research Grid (Westgrid) high performance computing cluster employing 100 or more processors. For the generation of particle phase spaces, the BEAMnrc simulations included models of a Varian 600C 6MV linac (Varian Medical Systems, Palo Alto, CA), the magnet poles, the yoke and the magnetic shields of the MRIs. The 6 MV photon beam source for the Varian 600C linac has been modeled and benchmarked against the measurements in a previous work.[18] Fig. 3.3(a) displays a schematic diagram of the simulated longitudinal RBP linac-MR assembly, with an isocenter at 126 cm distance from the linac target. The air gap is defined as the distance between the phantom surface and the magnet pole, and the air column refers to the ~46 cm hole in the yoke and pole plate. The transverse RBP linac-MR configuration was modeled by rotating the entire Linac and shielding structures by 90 degrees with respect to the magnet (see Fig. 3.1), and then displacing these objects 20 cm further away from isocenter (source to axis distance, SAD = 146 cm) than in the longitudinal configuration as described in the preceding section. The BEAMnrc code was used to calculate the phase space (i.e. particle type, position, directional vector, and energy) data. For the longitudinal configuration, phase space files were generated at the phantom

surface for radiation field sizes of 5x5, 10x10, 15x15, and 20x20 cm^2 at an air gap of 21.5 cm. The phase space calculations were then repeated for air gaps of 6.5, 11.5, 16.5, 21.5, 26.5, and 31.5 cm for a fixed 10x10 cm^2 field size. For the transverse geometry, phase spaces at a distance of 116 cm from the source (20 cm prior to the phantom surface) were simulated for field sizes of 5x5, 10x10, 15x15, and 20x20 cm^2. In both geometries, field size was defined at the machine isocenter. The number of particle histories (i.e. electrons impinging on the target) simulated for the longitudinal and transverse systems were 3 x 10^8 and 2 x 10^9 which resulted in a total of ~2.3 x 10^8 (with ~0.4% electrons) and ~1.4 x 10^9 (with ~0.3% electrons) particles in the phase-space files, respectively. Directional Bremsstrahlung splitting (DBS) was used with a splitting number of 1000. DBS is a variance reduction technique that uses a combination of interaction splitting for Bremsstrahlung, annihilation, Compton scattering, pair production and photoabsorption, and Russian Roulette to achieve high efficiency of photon beam treatment head simulations while making sure that the particles reach the scoring plane, i.e. phase space, with equal weight. The 3D MRI vector magnetic fields were incorporated in the BEAMnrc models in the calculation of the phase space files (see § 4.2.1).

With phase spaces for the different field size/air gap combinations for the two RBP linac-MR configurations as the source input, DOSXYZnrc was then used to score dose distributions in a 30 x 30 x 20 cm^3 water phantom (20 cm dimension along the photon beam direction). The central axis (CAX) percent depth-doses

were scored using 2 x 2 cm^2 x 70 μm (along beam direction) voxels for in phantom depths up to 1.0 cm, and 2 x 2 x 0.1 cm^3 voxels at greater depths. For simulations of the transverse geometry, the exit skin doses were also scored using 70 μm voxels in the depth direction in the last 1.0 cm depth of the phantom. A 2D dose distribution with lateral scoring resolution of 0.2 x 0.2 cm^2 was also generated for each of the 70 μm layers to study the entrance and exit doses in more detail. For the transverse geometry, the effect of variation in the angle of incidence, with respect to the patient surface, on entry and exit doses was also investigated. Entry and exit surface angles of -45°, -30°, -15°, 0°, +15°, 30°, 45° were simulated for a 10 x 10 cm^2 field size by rotating the water phantom about the systems' rotation axis (see Fig. 3.1) passing through the middle of the phantom at 10 cm depth. This was achieved by varying the parameter "theta" and setting the parameters "phi" and "phicol" to zero in the DOSXYZnrc input file. These parameters define the rotations of the phase space relative to the DOSXYZnrc coordinate system. For a head-first-supine patient, positive/negative surface angles then correspond to clockwise/counter-clockwise rotation of the linac gantry in a plane transverse to the cranial-caudal axis.
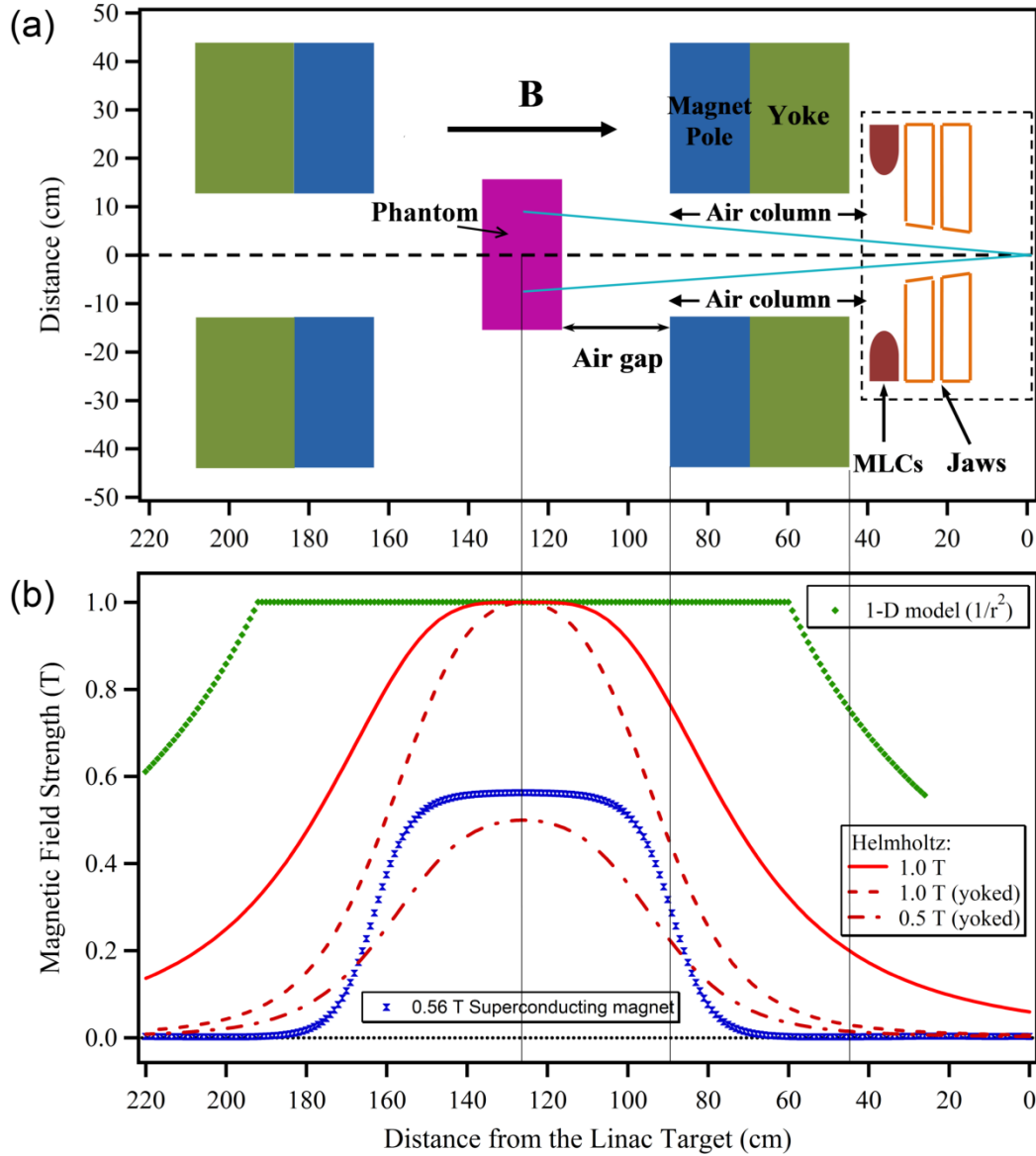
Figure 3.3: (a) Schematic diagram of the longitudinal linac-MR system with the isocenter at 126 cm. (b) The CAX magnetic field maps of our realistic 3D models versus a 1-D model.[19] The 1.0 T MRI of the 1-D model extends only to the end of the magnet in Fig. 2 of Ref [19].

The DOSXYZnrc simulations were run with 2 and 20 billion particle histories for the PDDs and 2D dose distributions, respectively, by recycling the phase-spaces

six times. Statistical uncertainties of less than 1% were achieved for all voxels in the PDD simulations. The 2D dose distributions had uncertainties of less than 1% within ±2 cm of the CAX, and no more than 3.5% elsewhere. Transport cut-off parameters for all EGSnrc simulations were set to AP=PCUT=0.01 MeV for photons. For electrons, cutoffs of AE=ECUT=0.521 MeV (rest mass + kinetic energy) were used in order to prevent prematurely terminating the transport of contaminant electrons.

3.2.1 Implementation of 3D Magnetic Fields

As discussed in previous works[11,12] the EGSnrc Monte Carlo simulations in the presence of a uniform magnetic field are performed by modifying the macro packages beamnrc_user_macros.mortran and emf_macros.mortran[13]. In this work these macros are further modified to read the discrete 3D B-field from a file and to interpolate for any particle position. These macros are only invoked after the completion of a conventional charged particle step, i.e. in the absence of the electromagnetic field. During a condensed-history transport step the exact trajectory of the particle is not modeled, nor are the exact forms of inelastic and multiple scattering forces known. Therefore, EGSnrc Monte Carlo implements the approximation that the deflections of electrons and positrons from inelastic scattering, multiple scattering, and from the external electromagnetic field can be decoupled.[17]   For accurate simulation of charged particle transport in electromagnetic fields, this approximation requires that the step sizes within the

71

condensed history algorithm be small enough to ensure that: (a) the relative change in the particle's kinetic energy remains small, (b) the change in the magnitude of the electromagnetic field across a step is small, and (c) the relative change in the particle's direction of motion is small. Condition (a) is easily satisfied in this work since the electric field is absent and the magnetic field does not change the particle's energy. Condition (b) is imposed in emf_macros.mortran by a macro that restricts the maximum change in the magnetic field to[13,17]

$$\frac{0.02 \times s}{|\vec{B}(\vec{r}_f) - \vec{B}(\vec{r}_0)|/|\vec{B}(\vec{r}_0)|},$$ (3.1)

where s is the conventional step size, $\vec{r}_0$ and $\vec{r}_f$ are the positions of the particle at the beginning and end of the step, and the value 0.02 is a user-defined parameter that sets a 2% upper limit on the amount of change of the magnetic field over the transport step. Condition (c) is imposed by a macro that restricts the maximum step size to[13,17]

$$\frac{0.02 \times m_e c^2 \times \beta(E_0)\gamma(E_0)}{q_e c \times |\vec{B}_\perp|},$$ (3.2)

where $m_e c^2$ is the electron's rest energy, c is the speed of light, q_e is the charge of an electron, $\beta(E_0)$ and $\gamma(E_0)$ are the familiar relativistic factors, E_0 is the electron's energy at the start of the step, $|\vec{B}_\perp|$ is the magnitude of the magnetic field perpendicular to the electron track. The value 0.02 is again a user-defined parameter corresponding to a maximum 2% change in direction over the transport

step. Condition (c) will be violated for electrons undergoing large angle deflections introduced by multiple scattering. However, the error introduced is negligible except in high-Z media subjected to strong magnetic fields.[17]

3.2.2 Benchmarks

Raaijmakers *et. al*[20] have experimentally verified GEANT4 Monte Carlo simulations of MRI-linac dose effects in the transverse geometry: the reduction in the build-up distance, the asymmetry of the lateral dose profile in the direction orthogonal to the magnetic field, and the dose increase at tissue-air interfaces due to returning electrons. GafChromic film measurements were performed for 5x5 cm^2, 10x10 cm^2, and 15x15 cm^2 6MV photon fields and in the presence of 0, 0.6 and 1.3 T magnetic fields. Depth-dose curves were measured in a PMMA-air-PMMA phantom and the lateral profiles were measured in a homogeneous PMMA phantom. The measurement results confirmed the accuracy of GEANT4 Monte Carlo simulations of these MRI-linac specific dose effects: the relative agreements between measurements and simulations were within 2.2%/1.8 mm and 2.3%/1.7 mm for the depth-dose curves and the lateral profiles, respectively (values represent gamma index criteria).

The accuracy of the magnetic field implementation in the EGSnrc Monte Carlo simulations presented in this work was verified by benchmarking electron trajectories against results generated using the GEANT4 Monte Carlo package

and the FEM package Opera-3D. The trajectory simulations were performed in vacuum to eliminate medium interactions, in a volume measuring 60 x 60 x 126 cm^3. The trajectories of electrons, initially with a purely longitudinal (z-directed) momentum, were calculated in both uniform and complex 3D magnetic fields. In the first comparative study, the gyration radius r_g of an electron with a given kinetic energy (varied from 0.1 to 10.0 MeV) in the presence of a uniform magnetic field (varied from 0.005 to 5.0 T) was determined from each simulation and r_g was compared against the analytical prediction,[21]

$$r_g = \frac{p_\perp(\text{MeV/c})}{3.00\,B(\text{T})}, \tag{3.3}$$

where $p_\perp$ is the component of the electron's momentum perpendicular to the magnetic field lines, c is the speed of light, and B is the field strength in Tesla.

The second benchmarking study used a hypothetical full 3D magnetic field defined as

$$B_x = B_y = 0.01 \times \exp(-0.1z) \tag{3.4a}$$

$$B_z = \begin{cases} 0.15\,\exp[-(80-z)] & \text{if } z \le 80 \\ 0.15 & \text{elsewhere} \end{cases} \tag{3.4b}$$

In Eqs. 3.4a and 3.4b, B_x, B_y, and B_z are the x, y, and z components of the magnetic field in Tesla while z is the z-coordinate (cm) along the initial direction of electron's momentum. A 0.5 MeV electron initially travelling in the

74

longitudinal (z-) direction was tracked in the presence of this 3D magnetic field. The B-field was calculated externally for a rectilinear grid with a grid spacing of 1 cm in all directions and then was incorporated into the EGSnrc and GEANT4 simulations. The interpolation algorithm used in both EGSnrc and GEANT4 to calculate the magnetic field at an arbitrary point from the rectilinear magnetic field map was also used to interpolate the magnetic fields at each of Oper-3D's irregularly spaced FEM mesh nodes. The electron trajectories from the various simulations were then extracted and compared.

3.3 REFERENCES

1. Comsol Multiphysics, ver. 3.4 (Comsol AB, Stockholm, 2007).

2. Opera-3D, ver. 13.0 (Vector Fields, Oxford, 2007).

3. M. J. Barnes, G. S. Clark, and M. Sassowsky, Three dimensional field calculations compared to magnetic measurements for BV1 and BV2 transfer line magnets, CERN SL–Note–98–063 MS.

4. S. Hojo, M. Kanazawa, K. Tashiro, *et al.*, Design study of magnetic channel at NIRS-AVF930, Proceedings of CYCLOTRONS, Lanzhou, China, 215–217, (2010).

5. V. I. Klyukhin, A. Ball, F. Bergsma, et al., Measurement of the CMS Magnetic Field, *IEEE Trans. Appl. Supercond.*, 18(2), 395–398 (2008).

6. S. Pittaluga, S. Besio, V. Punzo, A Trequattrini, "Racetrack coils for dedicated MRI magnets," IEEE Trans. Appl. Supercond. 20(3), 786–789 (2010).

7. N. B. S. Gloria, M. C. L. Areiza, I. V. J. Miranda and J. M. A. Rebello, "Development of a magnetic sensor for detection and sizing of internal pipeline corrosion defects," NDT E Int. 42, 669–677 (2009).

8. T. Tadic and B. G. Fallone, "Design and optimization of superconducting MRI magnet systems with magnetic materials," IEEE Appl. Supercond. 22, 4400107 (2012).

9. T. Tadic and B. G. Fallone, "Three-dimensional nonaxisymmetric pole piece shape optimization for biplanar permanent-magnet MRI systems," IEEE Trans. Magn. 47, 231–238 (2011).

10. T. Tadic and B. G. Fallone, "Design and optimization of a novel bored biplanar permanent-magnet assembly for hybrid magnetic resonance imaging systems," IEEE Trans. Magn. 46, 4052–4058 (2010).

11. C. Kirkby, T. Stanescu, S. Rathee, M. Carlone, B. Murray, and B. G.Fallone, "Patient dosimetry for hybrid MRI-radiotherapy systems," Med. Phys. 35, 1019–1027 (2008).

12. C. Kirkby, B. Murray, S. Rathee, and B. G.Fallone "Lung dosimetry in a linac-MRI radiotherapy unit with a longitudinal magnetic field," Med. Phys. 37, 4722–4732 (2010).

13. A. F. Bielajew, "The effect of strong longitudinal magnetic fields on dose deposition from electron and photon beams," Med. Phys. **20**, 1171–1179 (1993).

14. I. Kawrakow and D. W. O. Rogers, "The EGSnrc code system: Monte Carlo simulation of electron and photon transport," NRCC Report No. PIRS-701, 2003.

15. D. W. O. Rogers, B. Walters, and I. Kawrakow, NRCC Report No. PIRS-0509(A)rev I, 2005.

16. B. Walters, I. Kawrakow, and D. W. O. Rogers, NRCC Report No.PIRS-794rev B, 2005.

17. A. F. Bielajew, "Electron Transport in $\vec{E}$ and $\vec{B}$ Fields," in "Monte Carlo Transport of Electrons and Photons Below 50 MeV", eds. T. M. Jenkins, W. R. Nelson, A. Rindi, A. E. Nahum and D.W.O. Rogers, (Plenum Press) 421–434 (1989).

18. J. St. Aubin, S. Steciw, C. Kirkby, and B. G. Fallone, "An integrated 6 MV linear accelerator model from electron gun to dose in a water tank", Med. Phys. 37, 2279–2288 (2010).

19. B. M. Oborn, P. E. Metcalfe, M. J. Butson, A. B. Rosenfeld, P. J. Keall, "Electron contamination modeling and skin dose in 6 MV longitudinal field MRIgRT: Impact of the MRI and MRI fringe field," Med. Phys. 39, 874–890 (2012).

20. A. J. E. Raaijmakers, B. W. Raaymakers and J. J. W. Lagendijk, "Experimental verification of magnetic field dose effects for the MRI-accelerator", Phys. Med. Biol. 52, 4283–4291 (2007).

21. J. D. Jackson, *Classical Electrodynamics*, 3rd ed. (Wiley, Hoboken, 1999).

CHAPTER 4 : RESULTS AND DISCUSSION

4.1 REALISTIC 3D MAGNETIC FIELDS

In Fig. 3.3(b) the extension of the CAX B-fields is plotted with respect to the longitudinal linac-MR geometry. Our realistic 3D models exhibit fringe fields that rapidly fall off in the air column and drop to very small residual values as they enter the linac collimation system. The 0.56 T rotating bi-planar configuration, which is under installation by our group, has a fringe field with the most rapid fall off, dropping to 18 Gauss at the linac MLC. The generic yoked Helmholtz coil systems display fringe fields that drop to below ~240 Gauss at the linac MLC. The 1.0 T Helmholtz magnet without a yoke has a fringe field of ~0.19 T at the linac MLC, nearly 8-fold larger than the yoked Helmholtz fringe field, showing the significance of incorporating a yoke into the Monte Carlo simulations. For comparison an unrealistic 1-D model[1] of a 1.0 T MRI and a fringe field that varies as $1/r^2$ is shown. The 3D B-field of our RBP transverse geometry (not shown) has a main field of 0.56 T and a fringe field similar to that of the 0.56 T longitudinal configuration.

4.2   MONTE CARLO SIMULATIONS IN THE PRESENCE OF MAGNETIC FIELDS: BENCHMARKS

For each uniform magnetic field used in the first comparative study described earlier, the radius of curvature of the electron trajectories from both EGSnrc and GEANT4 deviates by less than 1% from the analytical prediction (Eq. 3.3) through at least five complete gyration cycles. Fig. 4.1(a) exhibits the electron trajectories obtained in the second comparative study with the full 3D magnetic field (defined by Eqs. 3.4a-b) being present. The electron trajectories from both the EGSnrc and GEANT4 are in very good agreement with the finite element method prediction by Opera-3D. The discrepancy between different electron tracks is displayed in Fig. 4.1(b). Although there are no interactions in these Monte Carlo simulations done in vacuum EGSnrc and GEANT4 still use different algorithms to determine the size of the next electron step. Thus, the length of individual steps will be different for the two packages, and as a result the deflections are applied at different locations along the trajectories. Since the magnetic field is approximated to be constant over the course of each step and the deflection is calculated based only on the magnetic field at the end of each step the deflections themselves will also differ.   These discrepancies propagate throughout the simulation in vacuum resulting in a maximum cumulative difference of only 0.7 mm between each of these electron trajectories after 1.26 m of electron travel in the z-direction. This small cumulative difference verifies the

accuracy of the implementation of the 3D magnetic field and the sufficiency of
the step size sampling algorithm in our EGSnrc Monte Carlo simulations.
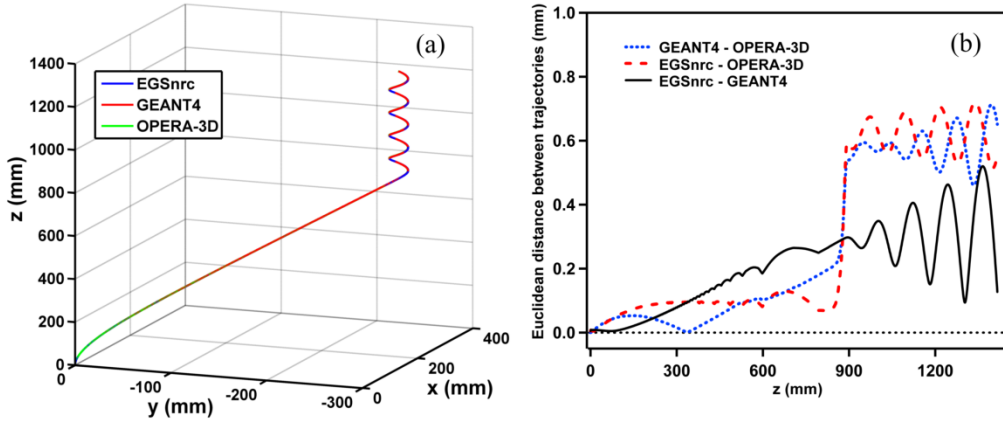
Figure 4.1: (a) The electron trajectories from the EGSnrc, GEANT4, and OPERA-3D are
shown in a 3D plot, where the electron originates at (0,0,0). (b) To compare each
electron trajectory in (a), the z-coordinate was fixed while the x- and y- coordinate of
each trajectory point was interpolated. Then, the Euclidean distances between the tracks
were calculated.

4.3 RBP LONGITUDINAL LINAC-MR SYSTEM

To quantify the confinement effect of different MR fringe fields on contaminant
electrons, we extracted the electron energy fluence spectra from phase-space files
for a 10x10 cm^2 field scored below the linac MLC, below the air column, and at
the phantom surface (21.5 cm air gap). Figure 4.2 depicts these spectra obtained
with (a) no magnetic field, (b) in the presence of our 0.56 T superconducting
magnet, and (c) for the 1-D (1/r^2) model.[1] In the absence of the magnetic field
there is a significant reduction of the electrons (scored in the 5x5 cm^2 central

region) from below the MLC to the end of the air column (~46 cm distance). This is simply due to the lateral scatter of the electrons in the air column that displaces a substantial number of electrons outside the scoring region. Similarly, a further, albeit smaller, reduction is observed within the 21.5 cm air gap. The energy fluence of the electrons below the MLC is essentially the same with and without our realistic 3D magnetic field (Figs. 4.2(a) and 4.2(b)), indicating that the confinement effect of the small fringe field penetrating the linac collimation system is insignificant. Interestingly, the realistic B-field somewhat reduces the energy fluence at the end of the air column, compared to the B = 0 T case. The exact cause of this reduction was not investigated, but may be explained by the fact that the x- and y- components of the 3D fringe field have rather complicated characteristics. Within the air gap, however, the 0.56 T MRI field clearly exhibits a confinement effect resulting in a small increase in the electron energy fluence below ~2.5 MeV. In the 1-D magnetic field model[1] a large fringe field encompasses the Linac collimation system and so most contaminant electrons generated anywhere in the Linac head, air column, and air gap are trapped and directed to the phantom surface with minimal lateral spread, giving rise to a "drastic" focusing of electrons in the center (Fig. 4.2(c)). It should be noted that the 1-D model focuses the electrons into a region smaller than 5x5 cm^2 and averaging over a smaller central area (e.g. 2x2 cm^2) would result in an even larger energy fluence (not shown here).
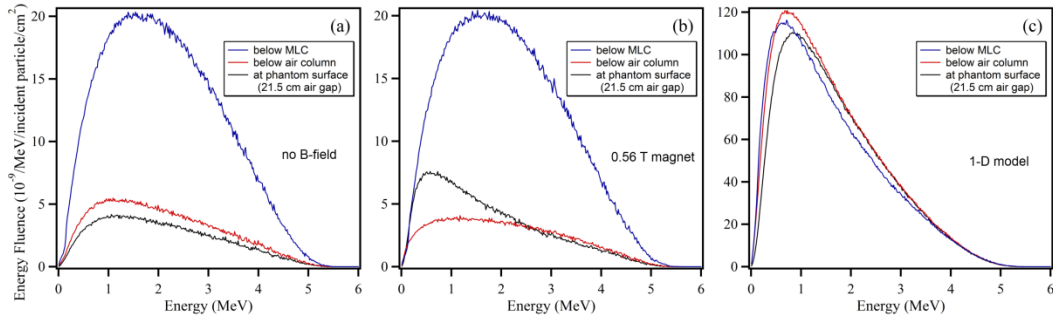
Figure 4.2: Energy fluence spectra of contaminant electrons for a 10x10 cm^2 field scored below the linac head (MLC), below the air column, and at the phantom surface (21.5 cm air gap) with (a) no magnetic field, (b) 0.56 T superconducting (CCI) magnet, and (c) 1-D ($1/r^2$) model.[1] These data were extracted from the central 5x5 cm^2 region of the phase-space. The energy fluences are normalized to the initial particle history in the Monte Carlo simulations.

4.3.1 Skin Dose in the Entry Region

Figure 4.3(a) displays the first 2 cm of the CAX percent depth-doses (PDD's) of a 10x10 cm^2 field delivered by a longitudinal linac-MR system with the magnetic fields of Fig. 3.3b, and the phantom surface placed normal to the beam at a 21.5 cm air gap. With the 1-D B-field model[1] an extreme skin dose of ~450% is observed, whereas with the realistic 3D models the skin doses are only slightly higher than the no B-field case (Fig. 4.3(b)). In the presence of the 0.5 and 1.0 T yoked Helmholtz fields the skin dose is approximately 1.5% higher than that of the 0.56 T superconducting systems, which is itself only ~ 8% larger that the skin dose when there is no magnetic field. However, the 1.0 T Helmholtz system without the yoke results in a ~65% skin dose, compared to ~21% for the yoked

system, which clearly indicates the necessity of incorporating the yoke in the magnetic field model in order to simulate a realistic field map.
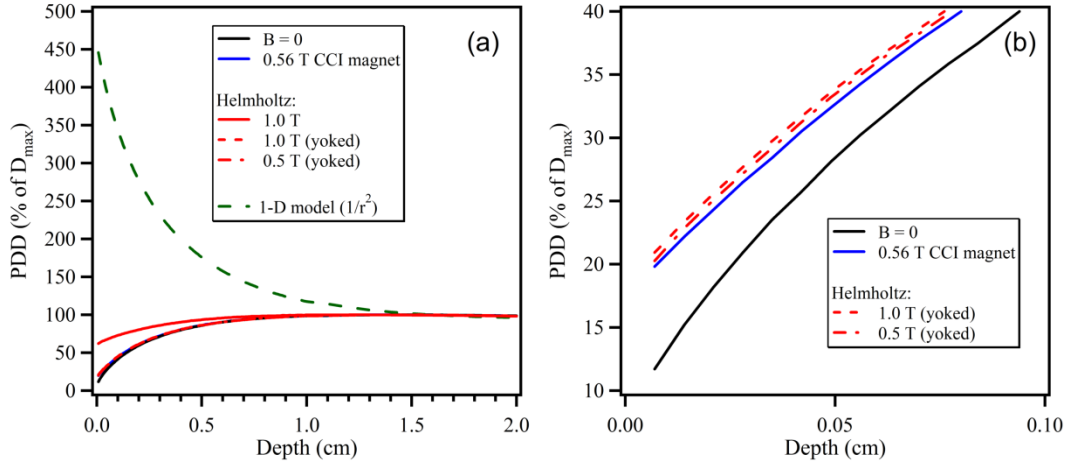
Figure 4.3: (a) First 2 cm of CAX PDD's for realistic 3D B-field models versus a 1-D model[1]. (b) Shows the magnification of the first 1 mm of (a). The data shown are for a 10x10 cm^2 photon beam and with the phantom surface at 21.5 cm air gap. A lateral voxel size of 2 cm was used for all B-fields.

The effect of the field size on the entry skin dose for our 0.56 T superconducting magnet linac-MR is compared to the same linac with zero magnetic field in Fig. 4.4. Line profiles through the middle of square fields of sizes from 5x5 to 20x20 cm^2 are shown in Fig. 4.4(a). The observed reduction of penumbra when the magnetic field is present is due to the Lorentz force confining the scattered electrons and focusing them parallel to the CAX. It is obvious that the increase in the skin dose due to the longitudinal B-field becomes smaller as the field size increases. The CAX entry skin dose as a function of field size is displayed in Fig. 4.4(b). In both zero and 0.56T B-field the phantom surface is positioned with a

84

21.5 cm air gap, and the skin dose is calculated as the dose deposited in the first 70 μm of the phantom. The increase in skin dose due to the magnetic field is greater for smaller field sizes, being 11% at 5x5 cm^2 and only 3% for a 20x20 cm^2 field. This is mostly due to the fact that with a small collimator there is a relatively large amount of contaminant electrons from the linac head (mostly flattening filter) that pass through or scatter off the jaws and are subsequently lost in the absence of the magnetic field, but are instead refocused in the presence of the longitudinal B-field. With a larger collimator the skin dose increase due to the longitudinal B-field is less pronounced, as a large portion of the contaminant electrons already contribute to the skin dose in the zero magnetic field case.

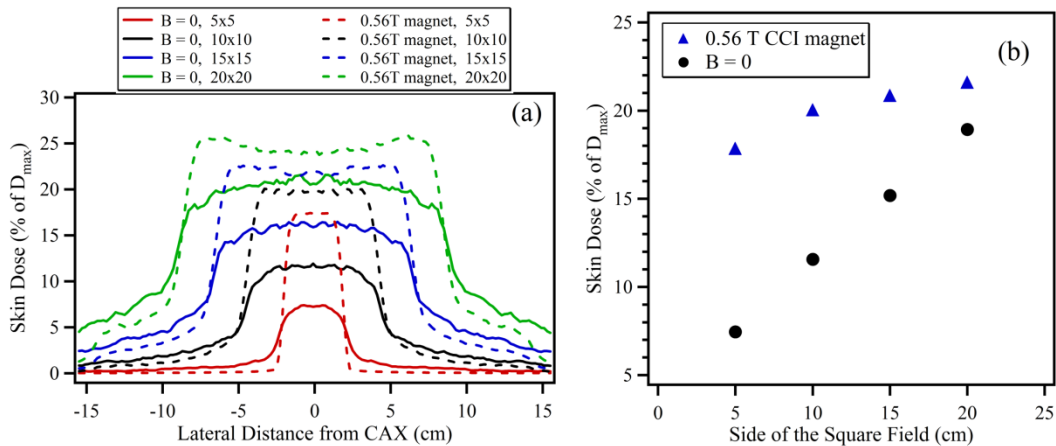**Figure 4.4:** (a) Entry skin dose line profiles through the CAX for our longitudinal linac-MR system in the presence/absence of the realistic 3D B-field model. (b) Comparison of the entry skin dose of the longitudinal linac-MR system with the 0.56T superconducting magnet to that without a magnetic field as a function of the field size (air gap of 21.5 cm). Lateral voxel sizes of 0.2 and 2 cm were used in (a) and (b) respectively.
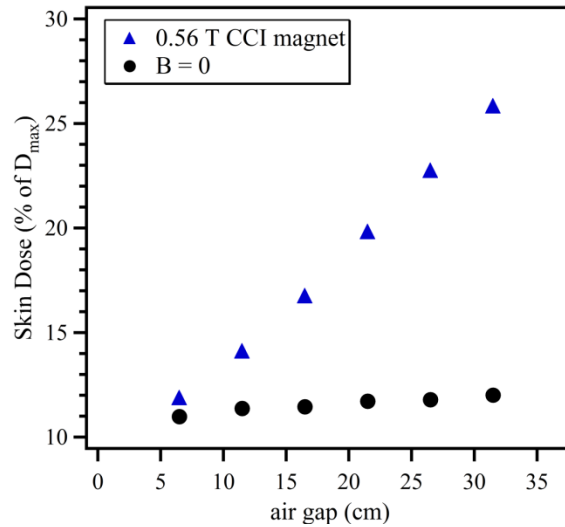
Figure 4.5: Comparison of the entry skin dose of the longitudinal linac-MR system with the 0.56T superconducting magnet to that without a magnetic field as a function of the air gap (field size of 10x10 cm^2). A lateral voxel size of 2 cm was used for all air gaps.

In Fig. 4.5, the dependence of the skin dose increase on the size of the air gap is illustrated. At the smallest air gap of 6.5 cm in this study, the effect of the magnetic field is to increase the skin dose by only 1 % from 11 % (no B-field) to 12 % (with B-field). The fact that the skin doses are nearly identical close to the magnet pole (zero air gap) confirm that the fringe fields of our realistic MRI systems have minimal effect on the skin dose since they do not significantly penetrate the Linac collimation system. With increasing air gap, there is very little change in the skin dose in the no B-field case, while in the presence of the B-field there is an approximately linear increase with air gap, up to 25% at the largest air gap of 31.5 cm. This linear increase with gap size is consistent with the majority of additional contaminants being produced in the air gap. Nevertheless, even up to

86

the largest air gap, the increase in skin dose due to the magnetic field is less than 13%.

4.4 RBP TRANSVERSE LINAC-MR SYSTEM

4.4.1 Skin Dose in the Entry Region

4.4.1.1 Perpendicular Beams

Figure 4.6(a) displays the CAX PDDs of a perpendicular (zero surface angle) 10x10 cm^2 photon beam incident on a 30 x 30 x 20 cm^3 phantom with and without the 0.56 T transverse magnetic field. On the entry side both the skin dose and the first 4 mm of the depth dose are slightly lower than the no B-field case (Fig. 4.6(b)). This is due to the magnetic field purging electron contamination from the beam path. As discussed previously by Oborn[1], a field strength of 0.6 T sweeps out most of the contaminant electrons and the resultant skin dose is very close to that of a contaminant-free simulation, where only dose from photons incident on the phantom surface is scored. Also, the Lorentz force perturbation of the secondary electrons produced in the phantom entry region has minimal effect on the skin dose. Figure 4.6(a) further shows that there is no shift in d_{max} to a shallower depth for this field strength.[2,3]
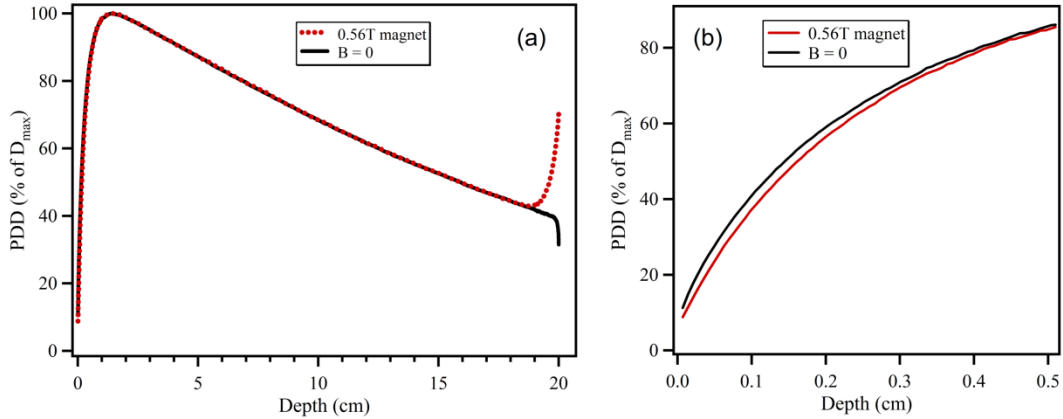
Figure 4.6: (a) The CAX PDD of our transverse linac-MR system in the presence of the realistic 3D B-field model. (b) The magnification of the first 5 mm of (a) is displayed. The data shown are for a 10x10 cm^2 photon beam and with the phantom surface at 136 cm from the linac source.

The effect of the field size on the entry skin dose is shown in Fig. 4.7. Line profiles through the middle of square fields of sizes from 5x5 to 20x20 cm^2 are shown in Fig. 4.7(a) for the no magnetic field and 0.56 T transverse magnetic field cases, illustrating the reduction of penumbra when the magnetic field is present. The CAX entry skin dose values are plotted as a function of field size in Fig. 4.7(b). For the smallest 5x5 cm^2 field size, the CAX skin dose is nearly the same with and without the magnetic field. As the field size is increased, both the zero magnetic field and 0.56 T field cases show an approximately linear increase in skin dose, but the 0.56 T case does so much more slowly. At a 20x20 cm^2 field size, the skin dose with the magnetic field is 7.5% less than that without magnetic field. This is consistent with the fact that a larger photon beam contains more contaminant electrons scattering off the linac head that contribute to skin dose.

88

Head-scattered electrons directed towards the patient surface generally do so at an angle with respect to the CAX, and under the influence of a transverse B-field they can be swept out of the central region on a helical path. Those electrons that would reach the surface parallel to the beam CAX will be deflected by the B-field on a circular path.

In the main B-field of 0.56 T, the gyration radius for the circular/helical path is ~ 0.9 cm for average electron energy of ~1 MeV, and no more than 3.9 cm, corresponding to electrons with the maximum electron energy of 6 MeV. Since the extension of the uniform main B-field above the patient surface will in general be significantly larger than these gyration diameters (as required for imaging), the electrons will remain on these helical paths that for a flat patient surface ("zero surface angle") will never intersect the patient surface. Hence, the purged electrons will not lead to an increased skin dose away from the field borders for this scenario ("zero surface angle"). This is supported by the lateral entry dose profiles shown in Figure 4.7(a), where there is no evidence of hot spots outside the field border. (Note that the profiles are shown with tails that extend a significant distance from the field borders in comparison to the estimated gyration radii, particularly for the smaller 5x5 and 10x10 cm^2 field sizes).
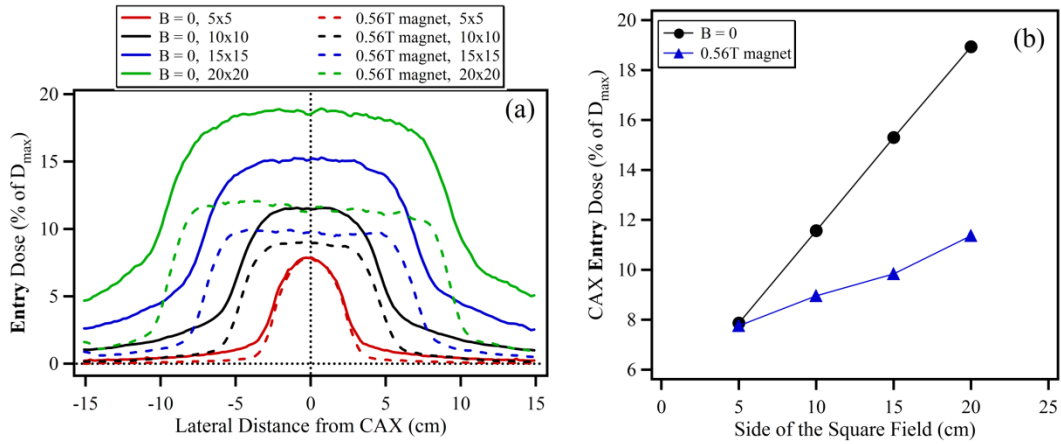
Figure 4.7: (a) Entry skin dose line profiles through the CAX and (b) entry skin dose as a function of the field size for our transverse linac-MR system in the presence of the realistic 3D B-field model. The phantom surface is at 136 cm from the linac source. Lateral voxel sizes of 0.2 and 2 cm were used in (a) and (b) respectively.

For a scenario where the surface is not flat, such as a neck tumor, electrons swept from a perpendicular beam could irradiate the chin and the chest leading to an increase in the skin dose. This would be similar to the skin doses for positive/negative surface orientations discussed in Section 4.4.1.2 and shown in Fig. 4.8.

4.4.1.2 Oblique Beams

The effect of angle of obliquity of the incident beam with respect to the phantom surface on the CAX entry skin dose is shown in Fig. 4.8 for a 10x10 cm^2 field size. In the absence of the magnetic field the skin dose increases with greater obliquity. This behaviour is well-known and was first explained in Ref. [4] using the concept of electron range surface (ERS). Figure 4.9 depicts a schematic of

90

ERS: secondary electrons generated in an element of volume at point Q will reach point P on the surface of the phantom if their range is greater than the distance QP. For the photon energies in this study the Compton scattering process predominates, hence both the energy and range of the electrons scattered at any particular angle are known. Therefore, one can construct an electron range curve such that those electrons generated inside the curve will reach point P and contribute to the skin dose, while those generated outside the curve make no contribution. The revolution of the electron range curve about the X-ray beam CAX will create a three-dimensional volume referred to as the electron range surface. The shape of the ERS and the volume it encompasses determines the skin dose at point P. Figure 4.9 clearly showing that the proportion of the secondary electrons in the phantom contributing to the skin dose increases with the angle of obliquity. The increase is symmetric for positive and negative angles and is steeper for angles larger than 30°. The increase in skin dose with larger angles of obliquity is more dramatic when the B-field is introduced. For angles within approximately $\pm20^{\circ}$ off perpendicular, the skin dose for the 0.56 T case remains smaller than that for the no field B-field case, but beyond $\pm20^{\circ}$ the presence of the magnetic field results in larger skin doses.

The relationship between the entry skin doses of the 0 T and 0.56 T cases is a manifestation of two competing processes: 1) purging of the contaminant electrons due to the transverse B-field, and 2) the Lorentz force perturbation (confinement) of the secondary electrons in the phantom contributing to the skin

dose. The first of these processes dominates for angles less than $\pm20^{\circ}$ and the latter for larger oblique angles. Regardless, even at large angles of obliquity the increase in skin dose for the 0.56 T case is still very modest, increasing by only 9% (from 18% to 27% of D_{max}) at 45°.
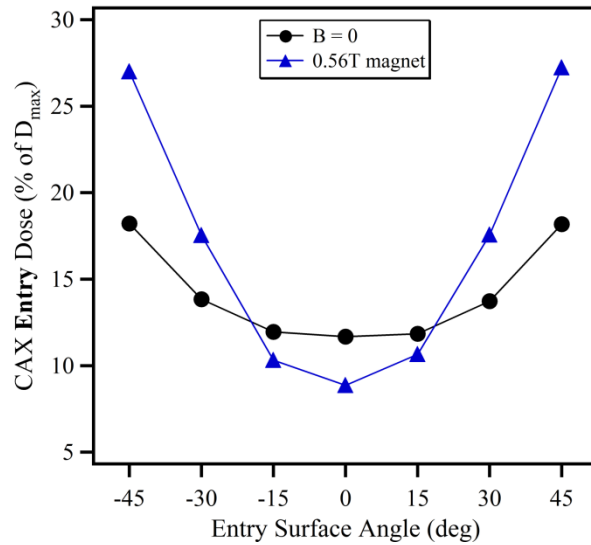
Figure 4.8: The CAX entry skin dose of the transverse linac-MR system as a function of the surface angle (non-perpendicular beams), for a 10x10 cm^2 photon beam. The surface of a 20 cm thick phantom was placed at a 136 cm distance from the linac electron gun (i.e. isocenter at 10 cm depth). A lateral voxel size of 2 cm was used for all surface angles.

Our results for positive surface angles are in good agreement with previous works by Raaijmakers[5,6] and Oborn[7] (0.6T B-field), but are in apparent contrast to their results for negative surface angles. As opposed to the symmetric behaviour we observe for our system, the entry skin dose in those works is lower than the 0 T case for all negative surface angles and exceeds the 0 T case for positive angles.

This is due to the major geometrical difference between the fixed cylindrical (FC) and rotating bi-planar (RBP) transverse configurations. Figure 1 of the work by Kirkby *et. al.*[8] shows the fundamental differences between the two systems. In the FC geometry, the Lorentz force acts perpendicular to the patient axis and its direction changes as the photon beam rotates around the patient in the transverse plane. While, in the RBP geometry the Lorentz force is along the superior-inferior patient axis for both positive and negative surface angles, leading to the observed symmetric behavior.
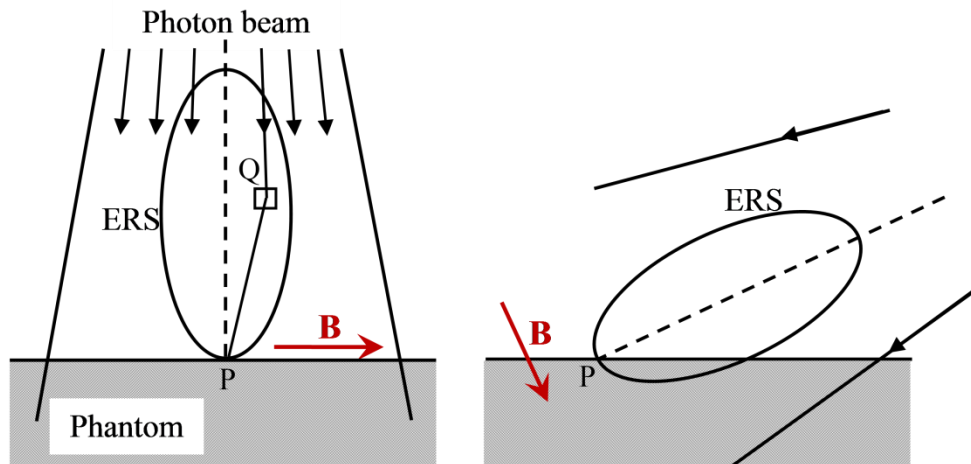
Figure 4.9: The contour of the Electron Range Surface for a photon beam in a linear accelerator. At an oblique angle of incidence there is a larger contribution of the secondary electrons generated in the phantom to the entry skin dose. Furthermore, the transverse magnetic field perturbs the path of these electrons and, hence, alters the entry skin dose.

4.4.2 Skin Dose in the Exit Region

4.4.2.1 Perpendicular Beams

In Fig. 4.6(a) the CAX PDDs of the perpendicular 10x10 cm^2 photon beam show an increase in the last 1 cm depth dose and in the exit skin dose (defined in the last 70 μm voxel) in the presence of the 0.56 T transverse magnetic field. This is due to the ERE occurring on the exit side.[7] The effect of the field size on the exit skin dose is shown in Fig. 4.10.
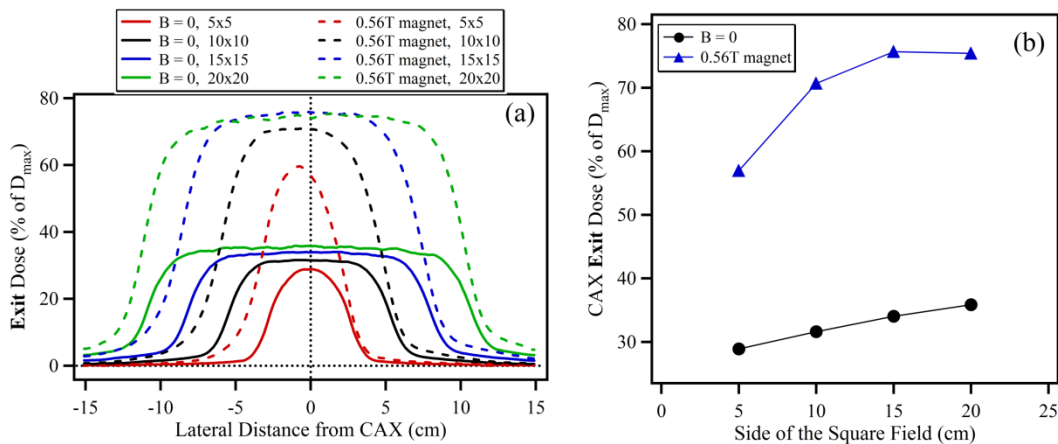
Figure 4.10: (a) Exit skin dose line profiles through the CAX and (b) exit skin dose as a function of the field size for our transverse linac-MR system in the presence of the realistic 3D B-field model. The phantom surface is at 136 cm from the linac source. Lateral voxel sizes of 0.2 and 2 cm were used in (a) and (b) respectively.

Unlike for the entry skin dose, where the centre of the fields did not shift in the presence of the transverse B-field, the line profiles of the exit skin dose shown in Fig. 4.10(a) are no longer symmetric about the CAX. This is due to the ERE shift,[7,9] which causes a displacement of the dose deposition. The spatial shifts in

the center of the line profiles are 9, 8.5, 7.5 and 5 mm for 5x5, 10x10, 15x15, and 20x20 cm^2 field sizes, respectively. It is observed, however, that for fields larger than 10x10 cm^2 the increased exit dose due to the magnetic field is fairly uniform within the shifted high dose region of the field. In other words, the shift in the high dose region does not cause the maximum dose point of the profile shift away from the CAX. This is not necessarily the case for a smaller field size; for example, the exit skin dose for, the 5x5 cm^2 field size at the CAX is smaller by 2.7% of D$_{max}$ than the maximum exit skin dose that occurs off CAX. It has been previously reported[5,7] that the movement of the maximum exit skin dose is primarily evident at small field sizes and low magnetic field strengths, where the average gyration radius of the returning electrons becomes comparable to half of the field size. For comparison, the gyration radii for 0.1, 0.5, 1.0, 2.0, and 6.0 MeV electrons traveling in air and perpendicular to a 0.56 T B-field are approximately 0.2, 0.5, 0.85, 1.5, and 3.9 cm respectively (Eq. (3.3)).

The magnitude of the maximum exit skin dose as a function of the field size is shown in Fig. 4.10(b). In the absence of the B-field, the exit skin dose ranges from ~28% to 34% of D$_{max}$, showing a slow linear increase with field size due to the larger contributions of lateral phantom scatter. With the 0.56T B-field the exit skin dose is significantly higher, ranging from ~56% to 73% of D$_{max}$. In this case the increase is not linear, with the skin dose reaching a maximum at the 15x15 cm^2 field size, and then levelling off. Oborn *et al.*[7] suggested that a significant reduction in the exit skin dose can be achieved by adding 1 cm thick exit bolus.

We would expect that the use of exit bolus would result in a similar reduction in our rotating bi-planar transverse linac-MR system, though this is not investigated in this work.

4.4.2.2 Oblique Beams

Figure 4.11 displays the maximum exit skin dose versus surface angle for the 10x10 cm^2 field size, with and without the 0.56 T transverse B-field. In the absence of the magnetic field the exit skin dose decreases for more oblique exit angles due to a decreased contribution of the secondary electrons in the phantom to the central region. This observed trend is reversed from what is observed at the entry side and again can be explain by means of electron range surface (Fig. 4.12).
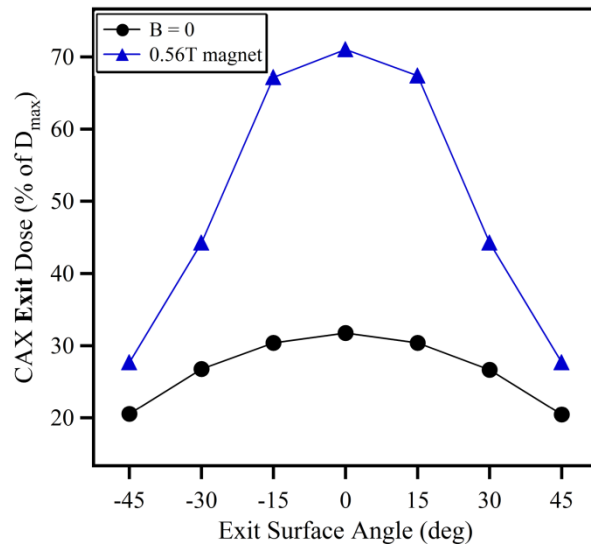
Figure 4.11: The CAX exit skin dose of the transverse linac-MR system as a function of the surface angle (non-perpendicular beams), for a 10x10 cm^2 photon beam. The surface of a 20 cm thick phantom was placed at a 136 cm distance from the linac target (i.e. isocenter at 10 cm depth). A lateral voxel size of 2 cm was used for all surface angles.

When the transverse B-field is introduced the exit skin dose also decreases for more oblique angles, as with the 0 T case, but remains larger than the 0 T case for all surface angles simulated. Within $\pm20^{o}$ off perpendicular, the reduction in the skin dose is quite gradual, but at larger oblique angles an abrupt decrease is observed. Whereas at perpendicular incidences, the exit skin dose is ~40% (of D_{max}) larger with the magnetic field, at oblique angles of 45° the 0.56 T exit dose is only 8% larger than the exit dose at 0 T. Similar to the entry skin dose a symmetric behaviour is observed on the exit side for positive and negative surface angles. On the exit side the two competing processes are: 1) the ERE which tends to increase the skin dose, and 2) a reduction in the secondary electrons generated in the phantom and above the exit layer, for more oblique surfaces. For the surface angles simulated the first effect always dominates, but to a lesser extent as the magnitude of the angle of obliquity increases (particularly above angles of 20°).
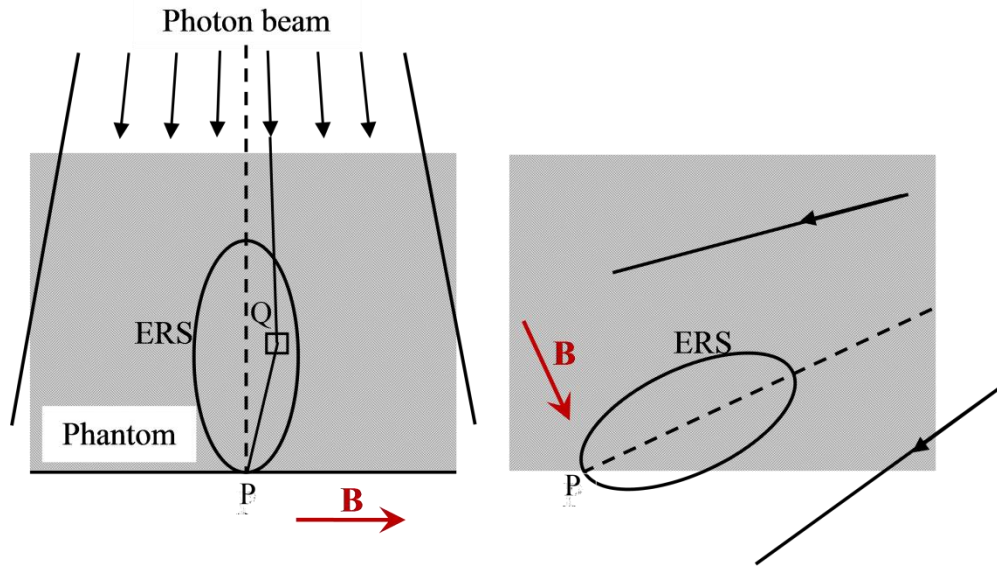
Figure 4.12: The contour of the Electron Range Surface for a photon beam in a linear accelerator. At an oblique angle of incidence there is a smaller contribution of the secondary electrons generated in the phantom to the exit skin dose. Furthermore, the transverse magnetic field perturbs the path of these electrons and, hence, alters the exit skin dose.

Similar to the entry side, our exit skin dose results for positive surface angles are consistent with previous works by Raaijmakers[5,6] and Oborn[7], but differ from their results for negative surface angles. As opposed to the symmetric behaviour we observed for our system the exit skin dose in those works tends to increase for negative surface angles up to about -30° and gradually drops beyond that. This difference is again due to the Lorentz force acting perpendicular to the patient axis in the fixed cylindrical geometry and acting in parallel with the patient axis in our rotating bi-planar system.

98

4.5 REFERENCES

1. B. M. Oborn, P. E. Metcalfe, M. J. Butson, A. B. Rosenfeld, P. J. Keall, "Electron contamination modeling and skin dose in 6 MV longitudinal field MRIgRT: Impact of the MRI and MRI fringe field", Med. Phys. **39**, 874–890 (2012).

2. B. W. Raaymakers, A. J. Raaijmakers, A. N. Kotte, D. Jette, and J. J. Lagendijk, "Integrating a MRI scanner with a 6 MV radiotherapy accelerator: Dose deposition in a transverse magnetic field", Phys. Med. Biol. **49**, 4109–4118 (2004).

3. B. M. Oborn, P. E. Metcalfe, M. J. Butson, A. B. Rosenfeld, "High resolution entry and exit Monte Carlo dose calculations from a linear accelerator 6 MV beam under the influence of transverse magnetic fields", Med. Phys. **36**, 3549–3559 (2009).

4. B. Walters, I. Kawrakow, and D. W. O. Rogers, NRCC Report No.PIRS-794rev B, 2005.

5. A. J. Raaijmakers, B. W. Raaymakers, and J. J. Lagendijk, "Magnetic-field-induced dose effects in MR-guided radiotherapy systems: Dependence on the magnetic field strength", Phys. Med. Biol. **53**, 909–923 (2008).

6. A. J. E. Raaijmakers, B. W. Raaymakers, S. van der Meer, and J. J. W. Lagendijk, "Integrating a MRI scanner with a 6 MV radiotherapy accelerator: impact of the surface orientation on the entrance and exit dose due to the transverse magnetic fields", Phys. Med. Biol. **52**, 929–939 (2007).

7. B. M. Oborn, P. E. Metcalfe, M. J. Butson, A. B. Rosenfeld, "Monte Carlo characterization of skin doses in 6 MV transverse field MRI-linac systems:

effect of field size, surface orientation, magnetic field strength, and exit bolus", Med. Phys. **37**, 5208–5216 (2010).

8.   C. Kirkby, T. Stanescu, S. Rathee, M. Carlone, B. Murray, and B. G.Fallone, "Patient dosimetry for hybrid MRI-radiotherapy systems", Med. Phys. **35**, 1019–1027 (2008).

9.   A. J. Raaijmakers, B. W. Raaymakers, and J. J. Lagendijk, "Integrating a MRI scanner with a 6 MV radiotherapy accelerator: Dose increase at tissue-air interfaces in a lateral magnetic field due to returning electrons", Phys. Med. Biol. **50**, 1363–1376 (2005).

CHAPTER 5 : CONCLUSIONS

In this work we used Monte Carlo simulations to accurately predict skin dose changes in 6 MV RBP longitudinal and transverse linac-MR systems. By using FEM we accurately modeled realistic 3D magnetic field maps of linac-MR systems that correctly predict the rapid decay of the fringe fields.

For the longitudinal geometry, simulations of the skin dose in the presence of generic Helmholtz coil systems prove the necessity of incorporating a yoke into the linac-MR model. The EGSnrc Monte Carlo simulations predict that realistic 3D longitudinal fields mostly confine contaminant electrons that are generated in the air gap in the central region, where the main magnetic field exists. The fringe fields are too small to cause appreciable confinement of electrons produced in either the air column or the linac head. Using realistic 3D MRI fields, longitudinal linac-MR systems will result in only a small increase in entrance skin dose. This is contrary to a previous report, which relied on the use of a variety of hypothetical 1-D forms for the magnetic field maps. The increase in the entrance skin dose of longitudinal linac-MRIs remains below 15% of D_{max} for all the simulated scenarios.

For the transverse geometry, the CAX entry skin dose is equal to or smaller than that of the zero B-field case for perpendicular beams. When a 10x10 cm^2 field is obliquely incident on a phantom, the presence of the magnetic field increases the

CAX entry skin dose by no more than 10% of D_{max} when the magnitude of the angle of obliquity is $\leq 45^o$, and in fact decreases the entry skin dose for angles $\leq$ 20°. On the exit side, the simulations suggest that the transverse magnetic field does increase the skin dose by up to 42% of D_{max} compared to the zero B-field case. The increase in exit skin dose is largest for perpendicular beams, but appreciably drops and approaches the zero B-field case for large oblique angles of incidence. The magnitude of the exit skin dose for our transverse RBP system is comparable to what has been previously reported by Oborn *et al.* for a cylindrical transverse geometry. Since in their work a 1 cm thick exit bolus was found to be a potential solution to significantly reduce the exit dose, we expect that a similar approach will be suitable for the transverse RBP linac-MR system.

Based on our results, we do not expect the changes in skin doses caused by the magnetic field of our RBP linac-MR to be a limitation in the use of the system in either the longitudinal or transverse geometric configurations.

BIBLIOGRAPHY

1. G. B. Arfken and H. J. Weber, Mathematical Methods for Physicists, 6th ed. (Elsevier, Burlington, 2005). (31)

2. J. St. Aubin, S. Steciw, C. Kirkby, and B. G. Fallone, "An integrated 6 MV linear accelerator model from electron gun to dose in a water tank", Med. Phys. 37, 2279–2288 (2010). (67)

3. M. J. Barnes, G. S. Clark, and M. Sassowsky, Three dimensional field calculations compared to magnetic measurements for BV1 and BV2 transfer line magnets, CERN SL–Note–98–063 MS. (62)

4. M. J. Berger, "Monte Carlo calculation of the penetration and diffusion of fast charged particles." In *Methods in Computational Phsyics, Volume I Statistical Physics*. B. alter, S. Fernbach, M. Rotenberg (Eds.). (New York: Academic Press), pp. 135−215, 1963. (45, 53)

5. H. A. Bethe, "Theory of passage of swift corpuscular rays through matter", Ann. Physik. **5**, 325 (1930). (45, 51)

6. H. A. Bethe, "Scattering of Electrons", Z. Phys. **76**, 293 (1932). (45, 51)

7. J. Bernier, E.J. Hall, and A. Giaccia, *Radiation oncology: a century of achievements*, Nature Reviews Cancer **4**, 737–747, 2004. (1, 2, 3, 4, 5, 6)

8. A. F. Bielajew, "The effect of strong longitudinal magnetic fields on dose deposition from electron and photon beams", Med. Phys. **20**, 1171–1179 (1993). (16, 67, 70, 72)

9. A.F. Bielajew, "Electron Transport in $\vec{E}$ and $\vec{B}$ Fields," in "Monte Carlo Transport of Electrons and Photons Below 50 MeV", eds. T.M. Jenkins, W.R.

Nelson, A. Rindi, A.E. Nahum and D.W.O. Rogers, (Plenum Press) 421–434 (1989). (17, 47, 59, 67, 70, 72)

10. F. Block, "Stopping power of atoms with several electrons", Z. Phys. **81**, 363 (1993). (45, 51)

11. Y. Chen, A. F. Bielajew, D. W. Litzenberg, J. M. Moran, and F. D. Becchetti, "Magnetic confinement of electron and photon radiotherapy dose: A Monte Carlo simulation with a nonuniform longitudinal magnetic field", Med. Phys. **32**, 3810–3818 (2005). (16)

12. Comsol Multiphysics, ver. 3.4 (Comsol AB, Stockholm, 2007). (62, 63)

13. W. D. Coolidge. United States Patent Office. (1934) *X-ray Tube,* US Patent 1946312. (2)

14. L. A. Dawson, D. A. Jaffray. Advances in Image-Guided Radiation Therapy. *Journal of Clinical Oncology* **25**(8) 938–946 (2007). (6, 9)

15. J. F. Dempsey, D. Benoit, J. R. Fitzsimmons, et al. "A Device for Real time 3D Image-Guided IMRT", *Int. J. Radiat. Oncol. Biol. Phys.*, **63,** S202−S202, (2005). (12)

16. J. F. Dempsey. An Image-Guided Device Providing 4D CINE MRI Simultaneous to Radiotherapy Delivery. *Journal of Radiotherapy in Practice* **5** 179 (2006). (12)

17. J. V. Dyk. *The Modern Technology of Radiation Oncology* (Medical Physics Publishing, Wisconsin, 1999 & 2005). (1, 2, 4, 5, 6)

18. G. Failla, *An objective method for the administration of X-rays*, Acta Radiologica, **4**, 85–128, 1925. (3)

19. B. Fallone, M. Carlone, B. Murray, S. Rathee, T. Stanescu, S. Steciw, K. Wachowicz, and C. Kirkby, "Development of a linac-MRI system for real-time ART", *Med. Phys.* 34, 2547 (2007).   (12, 13)

20. B. G. Fallone, B. Murray, S. Rathee, *et al.* "First MR images obtained during megavoltage photon irradiation from a prototype integrated linac-MR system", *Med. Phys.*, **36,** 2084−2088, (2009).   (12, 13)

21. O. Glasser. *Wilhelm Conrad Rontgen and the Early History of the Roentgen Rays* (C. C. Thomas, Illinois, 1934).   (1)

22. N. B. S. Gloria, M. C. L. Areiza, I. V. J. Miranda and J. M. A. Rebello, "Development of a magnetic sensor for detection and sizing of internal pipeline corrosion defects," NDT E Int. 42, 669–677 (2009).   (63)

23. D. J. Griffiths, Introduction to Electrodynamics, 3rd ed. (Prentice Hall, Upper Saddle River, 1999).   (28, 29, 30, 31)

24. V. N. Hansen, P. M. Evans, and W. Swindell, "The application of transit dosimetry to precision radiotherapy", *Med. Phys.* **23**(5), 713−721 (1996). (10)

25. M. van Herk. Errors and Margins in Radiotherapy. *Seminars in Radiation Oncology* **14**(1) 52–54 (2004).   (9)

26. J. D. P. Hoisak, K. E. Sixel, R. Tirona, P. Cheung, and J. P. Pignol, "Correlation of lung tumour motion with surrogates of respiration", *Med. Phys.* **31**(6), 1759 (2004).   (11)

27. S. Hojo, M. Kanazawa, K. Tashiro, *et al.*, Design study of magnetic channel at NIRS-AVF930, Proceedings of CYCLOTRONS, Lanzhou, China, 215–217, (2010).   (62)

28. G. S. Innes. "The one million volt X-ray therapy equipment at St. Bartholomew's Hospital", Br. J. Radiol., **22** (suppl), 11–16, (1988).   (2, 3)

29. International Commission on Radiation Units and Measurements, ICRU Report 50: Prescribing, Recording and Reporting Photon Beam Therapy (ICRU, Bethesda, 1993).   (7, 8)

30. International Commission on Radiation Units and Measurements, ICRU Report 62: Prescribing, Recording and Reporting Photon Beam Therapy (Supplement to ICRU Report 50) (ICRU, Bethesda, 1999).   (7, 8)

31. J. D. Jackson, Classical Electrodynamics, 3rd ed. (Wiley, New York, 1999).
                                        (29, 48, 74)

32. D. A. Jaffray, D. G. Drake, M. Moreau, A. A. Martinez, and J. W. Wong "A radiographic and tomographic imaging system integrated into a medical linear accelerator for localization of bone and soft-tissue targets", *Int. J. Radiat. Oncol*. **45**(3), 773−789 (1999).   (10)

33. D. A. Jaffray, J. H. Siewerdsen, J. W. Wong, and A. A. Martinez, "Flat-panel cone-beam computed tomography for image-guided radiation therapy", *Int. J. Radiat. Oncol*. **53**(5), 1337−1349 (2002).   (10)

34. J. Jin, The Finite Element Method in Electromagnetics, 2nd ed. (Wiley, New York, 2002).   (32, 33, 34, 37)

35. H. E. Johns and J. R. Cunningham. *The Physics of Radiology* (C. C. Thomas, Illinois, 1983).   (1, 2, 4)

36. A. Jones. "The development of megavoltage X-ray therapy at St. Bartholomew's Hospital". Br. J. Radiol., **22** (suppl), 3–10, (1988).   (3)

37. H. E. Johns and J. R. Cunningham. "A precision cobalt 60 unit for fixed field and rotation therapy", Am. J. Roentgenol. Radium Therapy Nuclear Med, **81**, 4–12, (1959). (5)

38. I. Kawrakow and D. W. O. Rogers, "The EGSnrc code system: Monte Carlo simulation of electron and photon transport," NRCC Report No. PIRS-701, 2003. (67)

39. D. W. Kerst. (1941). "The Acceleration of Electrons by Magnetic Induction". *Physical Review* **60**: 47–53. (3, 4)

40. W. Kilby, J. R. Dooley, G. Kuduvalli, S. Sayeh, and C. R. Maurer Jr., "The CyberKnife® Robotic Radiosurgery System in 2010", *Technology in Cancer Research and Treatment*, **9**(5), 433−452 (2010). (11)

41. J. G. M. Kok, B. W. Raaymakers, J. J. W. Lagendijk, J. Overweg, C. H. W. de Graaff and K. J. Brown. "Installation of the 1.5 T MRI accelerator next to clinical accelerators: impact of the fringe field", *Phys. Med. Biol.*, **54,** N409−N415, (2009). (12)

42. C. Kirkby, T. Stanescu, S. Rathee, M. Carlone, B. Murray, and B. G.Fallone, "Patient dosimetry for hybrid MRI-radiotherapy systems", Med. Phys. **35**, 1019–1027 (2008). (13, 14, 16, 67, 70, 93)

43. C. Kirkby, B. Murray, S. Rathee, and B. G.Fallone "Lung dosimetry in a linac-MRI radiotherapy unit with a longitudinal magnetic field", Med. Phys. **37**, 4722–4732 (2010). (13, 16, 67, 70)

44. T. Kitabatake and S. Takahashi. "Conformation Radiotherapy by Means of 6 MeV Linear Accelerator", Tohoku J. exp. Med., **94**, 37–43, (1968). (5)

45. V. I. Klyukhin, A. Ball, F. Bergsma, et al., Measurement of the CMS Magnetic Field, *IEEE Trans. Appl. Supercond.*, 18(2), 395–398 (2008).   (62)

46. Lagendijk, J.J.W., Raaymakers, B.W., Raaijmakers, A.J.E., et al. MRI/linac integration. *Radiotherapy and Oncology* **86** 25−29 (2008).   (12)

47. K. M. Langen, T. L. Jones, Organ motion and its management *Int. J. Radiation Oncology Biol. Phys.* **50**(1) 265–278 (2001).   (9)

48. K. M. Langen, S. L. Meeks, D. O. Poole, T. H. Wagner, T. R. Willoughby, P. A. Kupelian, K. J. Ruchala, J. Haimerl, and G. H. Olivera, "The use of megavoltage CT (MVCT) images for dose recomputations", *Phys. Med. Biol.* **50**(18), 4259−4276 (2005).   (11)

49. E. W. Larsen, "A theoretical derivation of the condensed history algorithm." Ann. Nucl. Energy **19**, 701−714 (1992).   (46)

50. J. S. Laughlin. "Development of the technology of radiation therapy". Radiographics, **9**, 1245–1266, (1989).   (2, 3, 4)

51. J. Lattanzi, S. McNeeley, W. Pinover, E. Horwitz, I. Das, T. E. Schultheiss, and G. E. Hanks, " A comparison of daily CT localization to a daily ultrasound-based system in prostate cancer", *Int. J. Radiat. Oncol.* **43**(4), 719−725 (1999).   (11)

52. J. Leong, "Use of digital fluoroscopy as an on-line verification device in radiation therapy", *Phys. Med. Biol.* **31**(9), 985−992 (1986).   (9, 10)

53. D. W. Litzenberg, B. A. Fraass, D. L. McShan, T. W. O. O'Donnell, D. A. Roberts, F. D. Becchetti, A. F. Bielajew, and J. M. Moran, "An apparatus for applying strong longitudinal magnetic fields to clinical photon and electron beams", Phys. Med. Biol. **46**, 401 (2001).   (16)

54. E. Lysholm, *Apparatus for the production of a narrow beam of rays in treatment by radium at a distance*, Acta Radiologica, 2, 516–519, 1923. (2)

55. T. R. Mackie, "History of tomotherapy", *Phys. Med. Biol.* **51**, R427–R453 (2006). (10)

56. T. R. Mackie, J. Kapatoes, K. Ruchala, W. G. Lu, C. Wu, G. Olivera, L. Forrest, W. Tome, J. Welsh, R. Jeraj, P. Harari, P. Reckwerdt, B. Paliwal, M. Ritter, H. Keller, J. Fowler, and M. Mehta, "Image guidance for precise conformal radiotherapy", *Int. J. Radiat. Oncol.* **56**(1), 89−105 (2003). (11)

57. G. Z. Moliere, "Theorie der Streuung Schneller Geladener Teilchen. I. Einzel-streuung am Abgeschirmten Coulom-Feld", Z. Naturforsch. **A2**, 133 (1947).

(45, 51)

58. G. Z. Moliere, "Theorie der Streuung schneller geladener Teilchen II Mehrfach-und Vielfachstreuung", Z. Naturforsch. **A3**, 78 (1948). (45, 51)

59. A. F. Monti, A. Ostinelli, M. Frigerio, et al. "An ICRU 50 radiotherapy treatment chart," Radiother. and Oncol., **35**, 145, (1995). (7)

60. O. Morin, A. Gillis, J. Chen, M. Aubin, M. K. Bucci, M. Roach, and J. Pouliot, "Megavoltage cone-beam CT: system description and clinical applications", *Med. Dosim.* **31**(1), 51−61 (2006). (10, 11)

61. B. M. Oborn, P. E. Metcalfe, M. J. Butson, A. B. Rosenfeld, "High resolution entry and exit Monte Carlo dose calculations from a linear accelerator 6 MV beam under the influence of transverse magnetic fields", Med. Phys. **36**, 3549–3559 (2009). (17, 87)

62. B. M. Oborn, P. E. Metcalfe, M. J. Butson, A. B. Rosenfeld, "Monte Carlo characterization of skin doses in 6 MV transverse field MRI-linac systems:

109

effect of field size, surface orientation, magnetic field strength, and exit bolus", Med. Phys. **37**, 5208–5216 (2010). (17, 92, 94, 95, 98)

63. B. M. Oborn, P. E. Metcalfe, M. J. Butson, A. B. Rosenfeld, P. J. Keall, "Electron contamination modeling and skin dose in 6 MV longitudinal field MRIgRT: Impact of the MRI and MRI fringe field", Med. Phys. **39**, 874–890 (2012). (18, 70, 79, 81, 82, 83, 84, 87)

64. Opera-3D, ver. 13.0 (Vector Fields, Oxford, 2007). (62, 63)

65. K. L. Pasma, B. J. Heijmen, M. Kroonwijk, and A. G. Visser, "Portal dose image (PDI) prediction for dosimetric treatment verification in radiotherapy. I. An algorithm for open beams", *Med. Phys.* **25**(6), 830−840 (1998). (10)

66. C.A. Perez, L.W. Brady, J.L. Roti "Overview" *Principles and Practice of Radiation Oncology 3rd Edition*, Editors: C.A. Perez and L.W. Brady, Philadelphia, PA: Lippincott-Raven, pp.1–78, 1998. (1)

67. S. Pittaluga, S. Besio, V. Punzo, A Trequattrini, "Racetrack coils for dedicated MRI magnets," IEEE Trans. Appl. Supercond. 20(3), 786–789 (2010). (62)

68. J. Pouliot, A. Bani-Hashemi, J. Chen, M. Svatos, F. Ghelmansarai, M. Mitschke, M. Aubin, P. Xia, O. Morin, K. Bucci, M. Roach, P. Hernandez, Z. R. Zheng, D. Hristov, and L. Verhey, "Low-dose megavoltage cone-beam CT for radiation therapy", *Int. J. Radiat. Oncol.* **61**(2), 552−560 (2005). (10)

69. B. W. Raaymakers, A. J. Raaijmakers, A. N. Kotte, D. Jette, and J. J. Lagendijk, "Integrating a MRI scanner with a 6 MV radiotherapy accelerator: Dose deposition in a transverse magnetic field", Phys. Med. Biol. **49**, 4109–4118 (2004). (16, 87)

70. B. W. Raaymakers, J. J. W. Lagendijk, J. Overweg, et al. "Integrating a 1.5 T MRI scanner with a 6 MV accelerator: proof of concept", *Phys. Med. Biol.*, **54,** N229−237, (2009).   (12, 13)

71. A. J. Raaijmakers, B. W. Raaymakers, and J. J. Lagendijk, "Magnetic-field-induced dose effects in MR-guided radiotherapy systems: Dependence on the magnetic field strength", Phys. Med. Biol. **53**, 909–923 (2008).

(16, 92, 95, 98)

72. A. J. Raaijmakers, B. W. Raaymakers, and J. J. Lagendijk, "Integrating a MRI scanner with a 6 MV radiotherapy accelerator: Dose increase at tissue-air interfaces in a lateral magnetic field due to returning electrons", Phys. Med. Biol. **50**, 1363–1376 (2005).   (16, 94)

73. A. J. E. Raaijmakers, B. W. Raaymakers, S. van der Meer, and J. J. W. Lagendijk, "Integrating a MRI scanner with a 6 MV radiotherapy accelerator: impact of the surface orientation on the entrance and exit dose due to the transverse magnetic fields", Phys. Med. Biol. **52**, 929–939 (2007).

(17, 92, 98)

74. A. J. E. Raaijmakers, B. W. Raaymakers and J. J. W. Lagendijk, "Experimental verification of magnetic field dose effects for the MRI-accelerator", Phys. Med. Biol. 52, 4283–4291 (2007).   (73)

75. E. Rietzel, S. J. Rosenthal, D. P. Gierga, *et al.* Moving targets: detection and tracking of internal organ motion for treatment planning and patient set-up. *Radiother. Oncol.* **73** S68–S72 (2004).   (9)

76. W. C. Roentgen. "On a New Kind of Rays", Nature, **53**, 274–276, (1896).

(1)

77. D. W. O. Rogers, B. Walters, and I. Kawrakow, NRCC Report No. PIRS-0509(A)rev I, 2005. (67)

78. K. J. Ruchala, G. H. Olivera, E. A. Schloesser, and T. R. Mackie, "Megavoltage CT on a tomotherapy system", *Phys. Med. Biol.* **44**(10), 2597−2621 (1999). (11)

79. P. G Seiler, H. Blattman, S. Kirsch, R. K. Muench, and C. Schilling "A novel tracking technique for the continuous precise measurement of tumour position in conformal radio therapy", *Phys. Med. Biol.* **45**(9), N103−N110 (2000).
(11)

80. H. Shirato, S. Shimizu, K. Kitamura, T. Nishioka, K. Kagei, S. Hashimoto, H. Aoyama, T. Kunieda, N. Shinohara, H. Dosaka-Akita, K. Miyasaka, "Four-dimensional treatment planning and fluoroscopic real-time tumor tracking radiotherapy for moving tumor", *Int. J. Radiat. Oncol.* **48**(2), 435−442 (2000).
(11)

81. T. Tadic. "Magnet design and optimization for an integrated linac-MRI system," Ph.D. thesis, (University of Alberta, 2012). (28, 31, 32, 37, 40)

82. T. Tadic and B. G. Fallone, "Design and optimization of superconducting MRI magnet systems with magnetic materials," IEEE Appl. Supercond. 22, 4400107 (2012). (64, 65)

83. T. Tadic and B. G. Fallone, "Three-dimensional nonaxisymmetric pole piece shape optimization for biplanar permanent-magnet MRI systems," IEEE Trans. Magn. 47, 231–238 (2011). (64)

84. T. Tadic and B. G. Fallone, "Design and optimization of a novel bored biplanar permanent-magnet assembly for hybrid magnetic resonance imaging systems," IEEE Trans. Magn. 46, 4052–4058 (2010). (64)

85. D. Verellen, M. De Ridder, N. Linthout, *et al*. Innovations in image-guided radiotherapy. *Nature Reviews Cancer* **7**, 949–960 (2007). (6, 9, 10)

86. B. Walters, I. Kawrakow, and D. W. O. Rogers, NRCC Report No.PIRS-794rev B, 2005. (67, 90)

87. A. B. Wayte. "Treatment of Some Disorders of the Pituitary by Radiotherapy", Proc R Soc Med, **44**, 450–452, (1951). (2)

88. T. P. Wangler. *RF Linear Accelerators* (Wiley-VCH, Weinheim, 2008). (4)

89. S. Webb. Motion effects in (intensity modulate) radiation therapy: a review. *Physics in Medicine and Biology* **51** R403–R42 (2006). (9)

90. C. X. Yu, C. J. Amies, and M. Svatos, "Planning and delivery of intensity-modulated radiation therapy", *Med. Phys*. **35**(12), 5233–5241, (2008). (5)

91. O. C. Zienkiewicz, R. L. Taylor, and J. Z. Zhu, The Finite Element Method: Its Basis and Fundamentals, 6th ed. (Elsevier, Oxford, 2005). (32, 36, 37)